RESEARCH ARTICLE

Cellular and Molecular Properties of Neurons

Ion-channel degeneracy and heterogeneities in the emergence of signature physiological characteristics of dentate gyrus granule cells

🔾 Sanjna Kumari and 🔾 Rishikesh Narayanan

Cellular Neurophysiology Laboratory, Molecular Biophysics Unit, Indian Institute of Science, Bangalore, India

Abstract

Complex systems are neither fully determined nor completely random. Biological complex systems, including single neurons, manifest intermediate regimes of randomness that recruit integration of specific combinations of functionally specialized subsystems. Such emergence of biological function provides the substrate for the expression of degeneracy, the ability of disparate combinations of subsystems to yield similar function. Here, we present evidence for the expression of degeneracy in morphologically realistic models of dentate gyrus granule cells (GCs) through functional integration of disparate ion-channel combinations. We performed a 45-parameter randomized search spanning 16 active and passive ion channels, each biophysically constrained by their gating kinetics and localization profiles, to search for valid GC models. Valid models were those that satisfied 17 sub- and suprathreshold cellular-scale electrophysiological measurements from rat GCs. A vast majority (>99%) of the 15,000 random models were not electrophysiologically valid, demonstrating that arbitrarily random ion-channel combinations would not yield GC functions. The 141 valid models (0.94% of 15,000) manifested heterogeneities in and cross-dependencies across local and propagating electrophysiological measurements, which matched with their respective biological counterparts. Importantly, these valid models were widespread throughout the parametric space and manifested weak cross-dependencies across different parameters. These observations together showed that GC physiology could neither be obtained by entirely random ion-channel combinations nor is there an entirely determined single parametric combination that satisfied all constraints. The complexity, the heterogeneities in measurement and parametric spaces, and degeneracy associated with GC physiology should be rigorously accounted for while assessing GCs and their robustness under physiological and pathological conditions.

NEW & NOTEWORTHY A recent study from our laboratory had demonstrated pronounced heterogeneities in a set of 17 electrophysiological measurements obtained from a large population of rat hippocampal granule cells. Here, we demonstrate the manifestation of ion-channel degeneracy in a heterogeneous population of morphologically realistic conductance-based granule cell models that were validated against these measurements and their cross-dependencies. Our analyses show that single neurons are complex entities whose functions emerge through intricate interactions among several functionally specialized subsystems.

complex systems; dendrite; degeneracy; heterogeneity; hippocampus

INTRODUCTION

The dentate gyrus (DG) is the gateway to the hippocampus proper and plays critical roles in engram formation, pattern separation, and spatial navigation. The granule cells are the principal excitatory neurons in the DG that receive afferent inputs from the entorhinal cortices through the perforant pathway and send outputs to the CA3 through the mossy fibers. Electrophysiological properties of DG granule cells and their dependencies on individual ion channels manifest pronounced heterogeneities (1–9). The use of a single hand-tuned model to computationally study granule cells would not accommodate such heterogeneities in characteristic physiological properties or the differential cross-dependencies across different physiological measurements. In addition, reliance on a single hand-tuned model would yield biased conclusions as the hand-tuned model is simply one instance of the several possible realizations of characteristic neuronal properties. The population-of-models approach is now an established route to systematically study heterogeneities and

differential dependencies of functional outcomes in several biological neuronal subtypes (10–27), including DG granule cells (1, 3, 5, 8).

The ability of disparate combinations of different ion channels to elicit similar signature physiological characteristics has been referred to as ion-channel degeneracy (11, 12, 28). There are several electrophysiological (4) and computational (1, 3, 5, 8) lines of evidence for the manifestation of ion-channel degeneracy in the manifestation of signature granule cell physiology. However, the lines of computational evidence for ion-channel degeneracy in DG granule cells come either from single compartmental models or without an extensive set of electrophysiological measurements that severely constrain the physiological outcomes. Morphologically realistic models with a broad set of physiological constraints are essential because morphology sets strong structural constraints on neuronal physiology (27, 29–32) and the number of physiological constraints contribute to model complexity (8, 33).

In this study, we build a population of GC models adapted from an extensive model (5) to demonstrate ion-channel degeneracy in morphologically realistic granule cell models that were biophysically and physiologically constrained. We used a systematic and unbiased search of a 45-parameter space that spanned all ion channels and their precise subcellular distributions. Importantly, we validated each random model using 17 different sub- and suprathreshold electrophysiological measurements from DG granule cells (2). We found a small subset (<1%) of 15,000 randomly generated morphologically realistic models to satisfy all 17 electrophysiological constraints. We performed quantitative analyses on the parametric and measurement spaces to demonstrate the manifestation of ion-channel degeneracy in the emergence of signature granule cell physiology. Together, these results reinforce existing lines of evidence for the manifestation of ion-channel degeneracy in DG granule cells, constrained by morphology, by ion-channel gating kinetics and distributions, and by several sub- and suprathreshold electrophysiological measurements.

Finally, we used this heterogeneous model population that manifested signature electrophysiological characteristics of DG granule cells to assess forward propagation of synaptic potentials and back-propagation of action potentials. We found the dendritic attenuation characteristics to be comparable with electrophysiological properties of granule cell dendrites, thus validating unconstrained measurements in our model population. Our analyses underscore the critical need to account for ion-channel degeneracy and heterogeneities in granule cells as they play crucial roles in defining their excitability, somatodendritic and dendro-somatic information transfer, and spatiotemporal summation.

METHODS

We adapted and retuned a morphologically and biophysically realistic DG granule cell (GC) model from Ref. 5 to match 17 different characteristic physiological properties of GCs (Fig. 1) from electrophysiological recordings (2). The GC morphology was stratified into seven sections: outer molecular layer (OML), middle molecular layer (MML), inner molecular layer (IML), granule cell layer (GCL), soma, axon initial segment (AIS), and axon. The stratification was implemented to nonhomogeneously distribute passive and active components

across different sections (Table 1), similar to the original model (5). Spines were implicitly accounted for by scaling the leak conductance and specific membrane capacitance in the IML by a factor of 1.45, and in the MML and OML by a factor of 1.9 (5). Leak channels were incorporated across sections nonhomogeneously (5, 34–36) by altering the leak conductance g_{pas} (Table 1).

There were 15 active conductances incorporated into the model, with their gating kinetics and distributions adapted and retuned from the original model (5) (Table 1; Fig. 1B). An inward-rectifier potassium channel (K_{ir}) (37–40) was set to be present in all sections, with location-dependent distribution of conductance. An eight-state sodium channel (Na) with region-dependent densities was incorporated into the model with the highest density in the AIS and lower densities in dendrites and soma (41, 42). Inactivating voltage-gated potassium channels $K_v1.1$ (43) and $K_v1.4$ (44) were present in AIS and axon, whereas $K_v4.2$ (45) was localized to dendrites. The delayed-rectifier $K_v3.4$ channels (46–50) were incorporated only into the axonal and AIS compartments. M-type potassium channels ($K_v7.2/7.3$) (51) were localized to the axon and the AIS. The hyperpolarization-activated cyclic nucleotide-gated (HCN) nonspecific cationic channels (52) were inserted in the dendrites. Voltage-gated N-type ($Ca_v2.2$) (53) and T-type calcium channels ($Ca_v3.2$) (54) were distributed across all compartments. Voltage-gated L-type calcium channels ($Ca_v1.2/1.3$) (55) were inserted such that $Ca_v1.3$ was present in all compartments and $Ca_v1.2$ spread across all sections except for the axon. The calcium-dependent big-conductance potassium (BK) channels (56) were inserted into the soma and axon. The calcium-dependent small-conductance potassium (SK) channels (57, 58) were incorporated in all the sections.

A majority of these ion channels were modeled using Hodgkin-Huxley dynamics (59). A-type $K_v4.2$ potassium channels followed a 15-state Markovian model. T-type $Ca_v3.2$ calcium and sodium channels were modeled as eight-state Markovian models. SK and K_{ir} channels were both modeled as six-state Markov models. Calcium buffer shell model was modified from Ref. 60. The Ca^{2+} decay time constant was set to 43 ms (61) in the axon and 240 ms (62) in all other compartments. Sodium reversal (E_{Na}) was set to 50 mV and potassium reversal (E_K) to –80 mV. Sodium channels (Na8st) were introduced in the dendritic compartments in GCL, IML, MML, and OML strata to accommodate active dendrites in GCs (63). All model parameters and their respective base values are listed section wise in Table 1.

Models were compartmentalized using the d_λ rule (64), whereby each compartment in the model was set to be less than 10% of the space constant of the neuronal section, computed at 100 Hz. This compartmentalization process yielded a total of 233 compartments in the base model, of which 163 were somatodendritic compartments.

Subthreshold Measurements

DG GC models were validated against 17 electrophysiological signature characteristics that were measured experimentally (2). The measurements were computed using well-established procedures (2, 4, 17, 26, 65, 66) that are detailed in the following paragraphs. Resting membrane potential (V_{RMP}) was measured as the potential at which the membrane rested when no current is injected. V_{RMP} was calculated
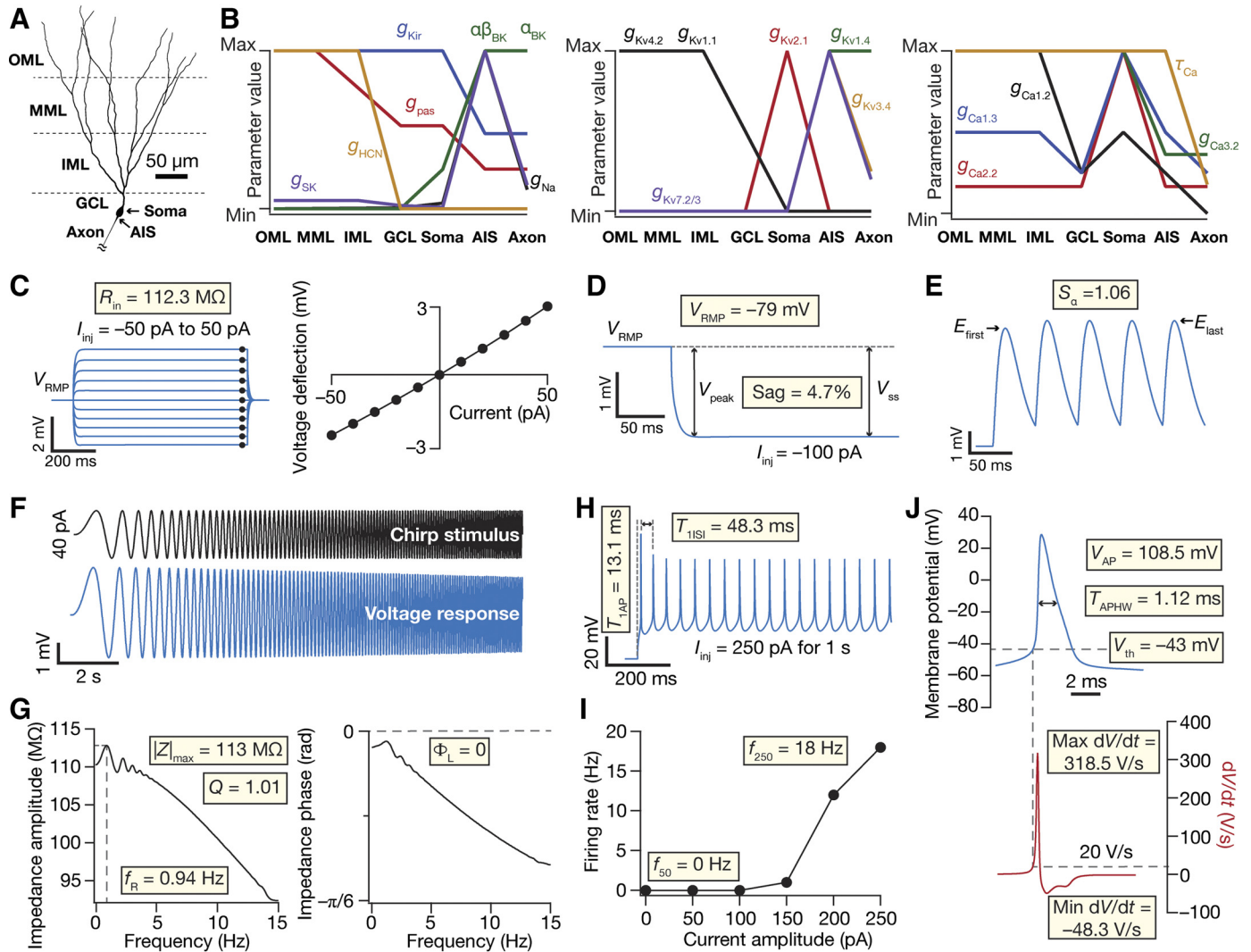
Figure 1. Morphologically realistic granule cell model showing signature physiological measurements. *A*: two-dimensional projection of the 3-D morphology of DG granule cell from Ref. 5. *B*: distribution of different ion-channel conductances across the morphological model of granule cells. *C, left*: somatic voltage traces recorded in response to the current injections (I_{inj}) of −50 pA to +50 pA in steps of 10 pA. *Right*, steady-state values of voltage responses from traces in the left plotted against the respective value of injected current. The slope of the linear fit on this plot yielded the input resistance (R_{in}) of the neuron. *D*: somatic voltage response to a 100 pA hyperpolarizing current injection. Sag was computed from the steady-state (V_{SS}) and peak (V_{peak}) values of voltage deflections from resting membrane potential (V_{RMP}). *E*: somatic voltage response to five alpha excitatory postsynaptic current injections to calculate summation ratio (S_{α}). *F*, *top*: chirp current stimulus spanning 0–15 Hz in 15 s of 40 pA peak-to-peak amplitude. *Bottom*, somatic voltage response to chirp current injection. *G*: impedance amplitude (*left*) and phase (*right*) profiles obtained from the chirp current stimulus and the associated voltage response in *F*. *H*: somatic voltage response showing action potential firing elicited by a 250-pA depolarizing current injection. *I*: plot of action potential firing rate against injected current amplitude, ranging from 0 to 250 pA in steps of 50 pA. *J*: first action potential from the train of spikes elicited by a 250-pA depolarizing current injection. The first derivative of the voltage response, dV/dt is plotted below. The voltage value at the time point where the derivative crossed 20 V/s was measured as threshold voltage V_{th}. AIS, axonal initial segment; GCL, granule cell layer; IML, inner molecular layer; MML, middle molecular layer; OML, outer molecular layer.

as the mean of recorded voltage for the last 50 ms of a 1-s simulation performed in the absence of current injection. All sub- and suprathreshold measurements were performed after an initial delay of 1 s to allow V_{RMP} to reach steady-state value. Input resistance (R_{in}) was measured as the slope of a linear fit to the steady-state *V*–*I* plot obtained by injecting subthreshold current pulses of amplitudes spanning from −50 to +50 pA, in steps of 10 pA (Fig. 1*C*). Percentage sag was measured from the voltage response of the cell to a hyperpolarizing current pulse of −100 pA for 1,000 ms and was defined as $100[1 − (V_{SS}/V_{peak})]$, where V_{SS} and V_{peak} depicted the steady-state and peak voltage deflection from V_{RMP}, respectively (Fig. 1*D*).

To assess temporal summation, five α-excitatory postsynaptic currents (α-EPSCs) with 50-ms interval were injected into the somatic compartment. Temporal summation ratio (S_{α}) was computed as E_{last}/E_{first}, where E_{last} and E_{first} are the amplitudes of last and first α-excitatory postsynaptic potentials, respectively, recorded in response to the injection of five α-EPSCs (Fig. 1*E*).

The chirp stimulus used for characterizing the impedance profiles was a sinusoidal current of constant amplitude below firing threshold, with its frequency linearly spanning 0–15 Hz in 15 s (Fig. 1*F*). The magnitude of the ratio of the Fourier transform of the voltage response (Fig. 1*F*) to the

Table 1. *Model parameters with their base values and the range spanned for the stochastic search algorithm for valid DG GCs*

Parameters/Sections	Soma	GCL	IML	MML	OML	AIS	Axon	Count
Passive properties								
Intracellular resistivity, R_a (Ωcm)								
Default value	200	200	200	200	200	200	100	2
Testing range (0.2–5×)	40–1,000	40–1,000	40–1,000	40–1,000	40–1,000	40–1,000	20–500	
Leak conductance, g_{pas} (μS/cm²)								
Default value	13.8	13.8	20.1	26.3	26.3	6.59	6.59	4
Testing range (0.2–5×)	2.76–69	2.76–69	4.02–100.5	0.46–131.5	0.46–131.5	1.32–32.95	1.32–32.95	
Active properties								
Na 8-state channel maximal conductance, g_{Na} (mS/cm²)								
Default value	18.8	2.8	2	1.25	1.25	540	65.18	6
Testing range (0.2–5×)	3.76–94	0.65–14	0.4–10	0.25–6.25	0.25–6.25	108–2700	13.01–325.9	
Inward rectifier K$^+$ channel maximal conductance, g_{Kir} (mS/cm²)								
Default value	0.354	0.354	0.354	0.354	0.354	0.168	0.168	2
Testing range (0.2–5×)	0.071–1.77	0.071–1.77	0.071–1.77	0.071–1.77	0.071–1.77	0.034–0.84	0.034–0.84	
Delayed rectifier K$^+$ channel maximal conductance, $g_{Kv2.1}$ (mS/cm²)								
Default value	70.91							1
Testing range (0.2–5×)	14.18–354.5							
Large conductance Ca^{2+}-activated potassium (*BK*) channel properties Maximum conductance alpha subu nit, α_{BK} (mS/cm²)								
Default value	15.6					62.4	62.4	2
Testing range (0.2–5×)	3.12–78					12.48–312	12.48–312	
Maximum conductance αβ subunit, $\alpha\beta_{BK}$ (mS/cm²)								
Default value	3.9					15.6	15.6	2
Testing range (0.2–5×)	0.78–19.5					3.12–78	3.12–78	
Small conductance Ca^{2+}-dependent potassium (SK) channel maximal conductance, g_{SK} (μS/cm²)								
Default value	0.83	1.67	4.37	4.37	4.37	83.3	12.5	5
Testing range (0.2–5×)	0.166–4.15	0.33–8.35	0.87–21.85	0.87–21.85	0.87–21.85	16.6–416.5	2.5–62.5	
N-type Ca^{2+} channel (Ca$_v$2.2) maximal conductance, $g_{Ca2.2}$ (mS/cm²)								
Default value	0.3	0.05	0.05	0.05	0.05	0.05	0.05	2
Testing range (0.2–5×)	0.06–1.5	0.001–0.25	0.001–0.25	0.001–0.25	0.001–0.25	0.001–0.25	0.001–0.25	
Ca^{2+} channel (Ca$_v$1.2) maximal conductance, $g_{Ca1.2}$ (mS/cm²)								
Default value	0.02	0.01	0.04	0.04	0.04	0.01		3
Testing range (0.2–5×)	0.004–0.1	0.002–0.05	0.008–0.2	0.008–0.2	0.008–0.2	0.002–0.05		
Ca^{2+} channel (Ca$_v$1.3) maximal conductance, $g_{Ca1.3}$ (mS/cm²)								
Default value	0.016	0.004	0.008	0.008	0.008	0.008	0.004	3
Testing range (0.2–5×)	0.0032–0.08	0.0008–0.02	0.0016–0.04	0.0016–0.04	0.0016–0.04	0.001–0.04	0.008–0.02	
T-type Ca^{2+} channel (Ca$_v$3.2) maximal conductance, $g_{Ca3.2}$ (mS/cm²)								
Default value	0.022	0.022	0.022	0.022	0.022	0.008	0.008	2
Testing range (0.2–5×)	0.0044–0.11	0.0044–0.11	0.0044–0.11	0.0044–0.11	0.0044–0.11	0.0016–0.04	0.0016–0.04	

Continued

Table 1.— *Continued*

Parameters/Sections	Soma	GCL	IML	MML	OML	AIS	Axon	Count
Ca Buffer–Ca decay constant, τ (ms)								
Default value	240	240	240	240	240	240	43	2
Testing range (0.2–5×)	48–1200	48–1200	48–1200	48–1200	48–1200	48–1200	8.6–215	
HCN channel maximal conductance, g_{HCN} (µS/cm²)								
Default value			4	4	4			1
Testing range (0.2–25×)			0.8–100	0.8–100	0.8–100			
K$^+$ channel (K$_v$1.1) maximal conductance, $g_{Kv1.1}$ (mS/cm²)								
Default value						0.25	0.25	1
Testing range (0.2–5×)						0.05–1.25	0.05–1.25	
K$^+$ channel (K$_v$1.4) maximal conductance, $g_{Kv1.4}$ (mS/cm²)								
Default value						10.12	10.12	1
Testing range (0.2–5×)						2.024–50.6	2.024–50.6	
K$^+$ channel (K$_v$3.4) maximal conductance, $g_{Kv3.4}$ (mS/cm²)								
Default value						30.78	7.66	2
Testing range (0.2–5×)						6.156–153.9	1.53–38.3	
A-type K$^+$ channel (K$_v$4.2) maximal conductance, $g_{Kv4.2}$ (mS/cm²)								
Default value		2.17	4.35	4.35	4.35			2
Testing range (0.2–5×)		0.43–10.85	0.87–21.75	0.87–21.75	0.87–21.75			
M-type K$^+$ channel (K$_v$7.2/3) maximal conductance, $g_{Kv7.2/3}$ (mS/cm²)								
Default value						6.7	1.34	2
Testing range (0.2–5×)						1.34–33.5	0.268–6.7	
Total Parameters								45

All channel names and their gating kinetics were taken from Beining et al. (5). The last column "Count" indicates the number of unique values associated with each parameter across the different sections. AIS, axon initial segment; DG, dentate gyrus; GC, granule cell; GCL, granule cell layer; IML, inner molecular layer; MML, middle molecular layer; OML, outer molecular layer.

Fourier transform of the Chirp stimulus yielded the impedance profile (66). The impedance amplitude profile was computed as:

$$|Z(f)| = \sqrt{(Re[Z(f)])^2 + (Im[Z(f)])^2}$$

where $Re[Z(f)]$ and $Im[Z(f)]$ were the real and imaginary parts, respectively, of the impedance Z as a function of frequency, f. The peak value of impedance across all frequencies was measured as the maximum impedance amplitude $|Z|_{max}$. The frequency at which the impedance amplitude reached its maximum value was defined as the resonance frequency (f_R). Resonance strength (Q) was measured as the ratio of the maximum impedance amplitude to the impedance amplitude at 0.5 Hz. Impedance phase $\phi(f)$ was computed as:

$$\phi(f) = \tan^{-1} \frac{Im[Z(f)]}{Re[Z(f)]}$$

Total inductive phase, Φ_L, defined as the area under the inductive part of $\phi(f)$ (Fig. 1G) was defined as (66):

$$\Phi_L = \int_{\phi(f) > 0} \phi(f) df$$

Suprathreshold Measurements

Suprathreshold measurements were obtained through depolarizing current injections, with amplitudes large enough to elicit action potentials (APs), into the cell resting at V_{RMP} (1, 2). AP firing frequency was computed by counting the number of spikes obtained during a 1,000 ms current injection (Fig. 1H). Current amplitude of these pulse-current injections was varied from 0 pA to 250 pA in steps of 50 pA, to construct the firing frequency versus injected current ($f - I$) plot (Fig. 1I). Various AP-related measurements were derived from the voltage response of the cell to a 250-pA pulse-current injection (Fig. 1, H and J). The temporal distance between the timing of the first spike and the time of current injection was defined as latency to first spike (T_{1AP}; Fig. 1H). The duration between the first and the second spikes was defined as the first interspike interval (T_{1ISI}). AP amplitude (V_{AP}) was computed as the difference between the peak voltage of the first spike and V_{RMP} (Fig. 1J). AP half-width (T_{APHW}) was the temporal width measured at the half-maximal points of the AP peak with reference to V_{RMP} (Fig. 1J). The maximum ($dV/dt|_{max}$) and minimum ($dV/dt|_{min}$) values were calculated from the temporal derivative of the first action potential obtained with 250-pA current injection (Fig. 1J). The voltage in the AP trace corresponding to the time point at which the dV/dt crossed 20 V/s was defined as AP threshold (V_{th}) (Fig. 1J). The sub- and suprathreshold measurements of the base model and their respective experimentally derived bounds are listed in Tables 2 and 3.

Multiparametric Multiobjective Stochastic Search

We used multiparametric multiobjective stochastic search (MPMOSS) (1, 10, 15–19, 21, 22, 25, 27, 67–75) to generate a heterogeneous population of GC neuronal models. A randomized search involving a parametric space of 45 dimensions (Table 1) was performed to generate valid models of GCs. Parameters whose distributions were nonidentical across

Table 2. *Subthreshold measurements of base model DG granule cells and their respective electrophysiological bounds*

Subthreshold Measurements	Base Model	Lower Bound	Upper Bound
Resting membrane potential, V_{RMP} (mV)	−79.93	−80	−70
Input resistance, R_{in} (MΩ)	112.34	90	300
Maximal impedance amplitude, $|Z|_{max}$ (MΩ)	112.81	90	225
Resonance frequency, f_R (Hz)	0.937	0.4	1.2
Resonance strength, Q	1.012	1	1.2
Total inductive phase, Φ_L (rad·Hz)	0	0	0.03
Sag (%)	4.7	1	7
Summation ratio of αEPSPs, S_α	1.06	0.9	1.5

Measurements were derived from Mishra and Narayanan (2). The bounds were designed to encompass ~90% of the respective electrophysiological measurement. It may be noted that all base model subthreshold measurements were within their respective bounds. DG, dentate gyrus.

sections were split into multiple parameters that depended on the section where they were placed. For example, K_{ir} channel has the same conductance value in the soma, GCL, IML, MML, and OML, but a different value for the axon and AIS. Thus, two parameters were defined for K_{ir} conductance, g_{Kir} 1 (soma, GCL, IML, MML, OML) and g_{Kir} 2 (axon and AIS).

The base model was hand-tuned to match most GC physiological characteristics (Fig. 1; Tables 1, 2 and 3). A total of 15,000 random morphologically realistic models were generated by sampling each base model parameters from respective uniform distributions that typically spanned 0.5–2× of their base values (Table 1). Specifically, we used 45 independent random number generators for picking each of the 45 parameters from their respective ranges (Table 1). This process was repeated 15,000 times to generate these random models. Sub- and suprathreshold physiological measurements of each model were computed (Fig. 1) and were validated against their respective bounds obtained from electrophysiological recordings from DG GCs (Tables 2 and 3). Models that satisfied all the 17 intrinsic measurement bounds (Tables 2 and 3) were declared valid.

Table 3. *Suprathreshold measurements of base model DG granule cells and their respective electrophysiological bounds*

Suprathreshold Measurements	Base Model	Lower Bound	Upper Bound
Firing frequency at 50 pA, f_{50} (Hz)	0	0	0
Firing frequency at 250 pA, f_{250} (Hz)	18	5	35
Action potential threshold, V_{th} (mV)	−42.92	−50	−30
Action potential amplitude, V_{AP} (mV)	108.539	100	
Action potential halfwidth, T_{APHW} (ms)	1.125	0.7	1.4
Peak dV/dt, $dV/dt|_{max}$ (V/s)	318.473	200	700
Minimum dV/dt, $dV/dt|_{min}$ (V/s)	−48.335	−160	−70
Latency to first spike, T_{1AP} (ms)	13.1	5	100
First interspike interval, T_{1ISI} (ms)	48.3	5	100

Measurements were derived from Mishra and Narayanan (2). The bounds were designed to encompass ~90% of the respective electrophysiological measurement. It may be noted that all base model suprathreshold measurements, except $dV/dt|_{min}$, were within their respective bounds.

Distance Measurements, Correlations, Dimensionality Reduction, and Clustering Analyses

The parameters and measurements of valid models were subjected to further analyses toward exploring heterogeneities and degeneracy. We computed pairwise Pearson's correlation coefficient (R) across parameters and measurements from all valid models. In addition, dimensionality reduction analyses on the measurements and the parametric spaces were performed with principal component analysis (PCA), t-distributed stochastic neighbor embedding (t-SNE) (76), uniform manifold approximation and projection (UMAP) (77), and potential of heat-diffusion for affinity-based trajectory embedding (PHATE) (78). To assess the presence of clusters in the parametric and measurement spaces, we used unbiased clustering through k-means clustering algorithm (79), independently for the parametric and the measurement spaces. The k-means clustering algorithm was used to assess clustering in the reduced dimensional space computed with t-SNE analysis and was visualized on the reduced t-SNE space. Then, these indices (with reference to the individual clusters) obtained from t-SNE clustering were projected on the other reduced dimensional spaces obtained with PHATE, UMAP, and PCA. This process was repeated with clustering performed on the reduced dimensional space of PHATE, UMAP, or PCA, with cluster indices projected to the three other reduced dimensional spaces.

To measure the distances between models, we used metrics that accounted for the widely variable ranges of the different model parameters (Table 1). The first distance metric we used in computing the distances between models was the Euclidean distance [$d_E(\mathbf{x}, \mathbf{y})$] computed between normalized parametric vectors $\mathbf{x} = (x_1, x_2, \cdots, x_{45})$ and $\mathbf{y} = (y_1, y_2, \cdots, y_{45})$ of two models:

$$d_E(\mathbf{x}, \mathbf{y}) = \sqrt{\sum_{i=1}^{45} (x_i - y_i)^2}$$

where normalization was performed for each parameter individually by rescaling its respective min–max range (Table 1) to 0–1. Thus, $0 \leq d_E(\mathbf{x}, \mathbf{y}) \leq \sqrt{45}$. The second distance metric that we used to compute distances between models was the Mahalanobis distance (80) that explicitly accounts for the covariance matrix of the underlying parametric distribution, thereby incorporating variance differences across the different model parameters into the distance measurements. The Mahalanobis distance [$d_M(\mathbf{x}, \mathbf{y})$] between the unnormalized parametric vectors $\mathbf{x}$ and $\mathbf{y}$ of two models was defined as:

$$d_M(\mathbf{x}, \mathbf{y}) = \sqrt{(\mathbf{x} - \mathbf{y})^T \sum{}^{-1} (\mathbf{x} - \mathbf{y})}$$

where Σ represented the covariance matrix across parameters spanning the entire distribution. Although the minimum value for $d_M(\mathbf{x}, \mathbf{y})$ would be 0, the maximum value would depend on the specific covariance matrix. To compute the maximum $d_M(\mathbf{x}, \mathbf{y})$, we constructed two parametric vectors $\mathbf{x}_{min}$ and $\mathbf{x}_{max}$, with each parametric value of these vectors, respectively, set to their respective minimum and maximum possible values from Table 1. We then assigned the distance d_M between $\mathbf{x}_{min}$ and $\mathbf{x}_{max}$, using the covariance matrix computed for the entire dataset, as the maximum possible distance (18, 22).

Synapse Model and Assessment of Backpropagating Action Potentials

Glutamatergic AMPAR synapses were placed in different model compartments with the following characteristics of granule cells (63, 81). The ionic current through these receptors was modeled using the Goldman–Hodgkin–Katz (GHK) convention (82–84). The intra- and extracellular concentrations for the different ions were set as: $[Na]_i = 18$ mM, $[Na]_o = 140$ mM, $[K]_i = 140$ mM, and $[K]_o = 5$ mM. These ionic concentrations ensured that the reversal potentials for AMPA receptors were set at 0 mV. The AMPAR current was modeled following the GHK convention, and was driven by sodium and potassium:

$$I_{AMPA}(v, t) = I_{AMPA}^{Na}(v, t) + I_{AMPA}^{K}(v, t)$$

where,

$$I_{AMPA}^{Na}(v, t) = \bar{P}_{AMPA} \, P_{Na} \, s(t) \, \frac{vF^2}{RT} \left(\frac{[Na]_i - [Na]_o \exp\left(-\frac{vF}{RT}\right)}{1 - \exp\left(-\frac{vF}{RT}\right)} \right)$$

$$I_{AMPA}^{K}(v, t) = \bar{P}_{AMPA} \, P_K \, s(t) \, \frac{vF^2}{RT} \left(\frac{[K]_i - [K]_o \exp\left(-\frac{vF}{RT}\right)}{1 - \exp\left(-\frac{vF}{RT}\right)} \right)$$

where $\bar{P}_{AMPA}$ defined the maximum permeability of the AMPA receptors, with $P_{Na} = P_K = 1$, R represented gas constant, and T was temperature in Kelvin. $s(t)$ governed the kinetics of the AMPA receptor current as follows:

$$s(t) = a \left(\exp\left(-\frac{t}{\tau_d}\right) - \exp\left(-\frac{t}{\tau_r}\right) \right)$$

where a defined a normalization factor that ensured $0 \leq s(t) \leq 1$. The rise and decay time constants of AMPAR were τ_r (= 2 ms) and τ_d (= 10 ms) (81). The AMPAR density (permeability value $\bar{P}_{AMPA}$) of individual synapses in the base model were adjusted (25–27, 31) such that the propagated somatic EPSP amplitude, irrespective of dendritic location, was in the 0.2–0.3 mV range to match with unitary somatic EPSP amplitudes in DG granule cells (63). The same location-dependent density values were used across all valid GC models to assess heterogeneities in synaptic information transfer within granule cells. A single synapse was placed in a somatodendritic compartment to measure the local EPSP amplitude as well the corresponding somatic EPSP amplitude resultant from dendro-somatic propagation. This procedure was repeated for all somatodendritic compartments across all valid GC models. The local and the somatic EPSP amplitudes were analyzed to assess heterogeneities in local EPSP amplitude and its somatic counterpart across different models.

Backpropagation of action potentials was assessed by initiating a single action potential at the soma (through a large pulse-current injection) and measuring the amplitude at different locations along the dendritic arbor. The recorded amplitudes from all somatodendritic compartments, for each valid GC, were analyzed to assess heterogeneities in backpropagation of action potentials.

Computational Details

All simulations were performed using the NEURON 7.2 programming environment (64) at 34°C, with temperature dependencies and Q_{10} values maintained from the original model (5). The simulation step size was set as 25 μs. Data analysis and plotting of graphs were done using custom-built software written in MATLAB or Igor Pro programming environment (WaveMetrics Inc.). Statistical analyses were performed in R (www.R-project.org). We used nonparametric statistical tests for statistical comparisons because the underlying data did not fit normal distributions. When there were more than two groups, we first performed Kruskal–Wallis test across all groups and then used Wilcoxon rank-sum test for individual pairs in the group. The actual P values obtained with the Kruskal–Wallis and the Wilcoxon tests are provided in the figures.

RESULTS

The aim of this study was to assess ion-channel degeneracy in morphologically realistic models of DG granule cells, which were constrained by a comprehensive set of sub- and suprathreshold electrophysiological measurements acquired in the laboratory (2). Toward this goal, we first adapted a detailed morphological model of granule cells from Ref. 5, whose biophysical properties (ion channel gating kinetics, distributions, and calcium handling mechanisms; Table 1) were derived from DG granule cells. We retuned this model to account (Fig. 1) for 17 different sub- and suprathreshold electrophysiological measurements recorded from granule cells (2). We introduced several changes to channel conductances and other properties in adapting the original model (Table 1). An important difference in our model was to account for active propagation of action potentials within granule cell dendrites (63) by incorporating spike-generating conductances into dendritic compartments. The hand-tuned base model matched the ranges of most (except for $dV/dt\,|_{\min}$; Tables 2 and 3) electrophysiological measurements (Fig. 1) and formed a substrate for generating a population of DG granule cells.

A Small Subset of Randomly Generated Models Satisfied All Signature Electrophysiological Characteristics of Granule Cells

To avoid biases associated with using a single hand-tuned model, we used a multiparametric multiobjective stochastic search (MPMOSS) algorithm over a large parametric space to identify valid GC models. The 45-dimensional parametric space spanned all ion-channel conductances and calcium handling across all spatial locations within the morphologically realistic model (Table 1). A total of 15,000 models were generated randomly by sampling independent uniform distributions associated with the 45 parameters, each spanning respective bounds (Table 1). Among these randomly generated models, valid GC models were those that satisfied all 17 sub- (Table 2) and suprathreshold (Table 3) electrophysiological measurements from granule cells (2). Each measurement required a different protocol and stimulus (or stimuli), which matched with their respective electrophysiological counterparts (2). Of the 15,000 random models, we found 141 (0.94%) to satisfy all 17 validation criteria (Tables 2 and 3). Thus, while arbitrary random combinations of the 45

parameters did not yield valid GC models (>99% models were invalid), there was a small subset of such combinations that yielded valid GC models. In what follows, we analyze the measurements and parameters associated with this subset of valid models to assess various aspects of their biophysical and physiological characteristics.

Pronounced Heterogeneities in and Weak Cross-Dependencies between Measurements from Valid Granule Cell Models Matched with Their Electrophysiological Counterparts

All 17 electrophysiological measurements were plotted for the 141 valid models (Fig. 2A) to assess if they were clustered or distributed across the range of their respective validation bounds (Tables 2 and 3). We found the 141 valid GC models to manifest heterogeneous physiological measurements (Fig. 2A), reflecting the heterogeneities observed in their biological counterparts (2). Expectedly, the firing rate for a 50-pA current injection, f_{50}, was identically zero for all models and two impedance measurements (resonance frequency, f_R, and total inductive phase, Φ_L) were clustered with low values (2). The low-pass nature of the granule cell impedance profile translates to low resonance frequency values and minimal inductive phase (2), thus resulting in clustered values for these measurements (Fig. 2A).

Turning to cross-dependencies across measurements in valid models, we asked if there were strong pair-wise correlations between these measurements. Strong pairwise correlations would either correspond to similar dependencies on the different ion channels or imply that the different measurements were not qualitatively distinct from each other and were capturing the same physiological characteristics. Although multiple measurements might be used to constrain models, a large number of strong pairwise correlations between these measurements would translate to insufficient constraints on the model validation process. We found a large majority of the pairwise Pearson's correlation values to be weak [between –0.4 to 0.4, defined as weak as per existing descriptions (85)] and nonsignificant (Fig. 2B). A small percentage of measurement pairs showed strong correlations, in a manner that was consistent with electrophysiological measurements from granule cells (2). Specifically, we found strong positive correlations between R_{in}, $|Z|_{\max}$, and S_{α}, similar to their dependencies in measurements from rat granule cells (2). This was expected because these subthreshold measurements of excitability are dependent on same sets of passive and active properties. We found strong negative correlation between $dV/dt\,|_{\max}$ and V_{th}, which was expected because the voltage threshold will be more hyperpolarized if the rate at which voltage rises toward 20 V/s is high (used in computing V_{th}; Fig. 1J). For all graphs, the number of valid models, $N_{valid} = 141$.

We applied linear and nonlinear dimensionality reduction techniques on the measurement space associated with the 141 valid models, the outcomes of which also did not suggest strong cross-dependencies across the different measurements in valid models (Fig. 3). Specifically, the reduced dimensional projections associated with nonlinear (Fig. 3, A–C) and linear (Fig. 3D) dimensionality reduction techniques did not visually manifest clusters. Although some projections showed broad distributions spanning the reduced dimensional space (Fig. 3, A and D), certain others suggested the possibility of a low-
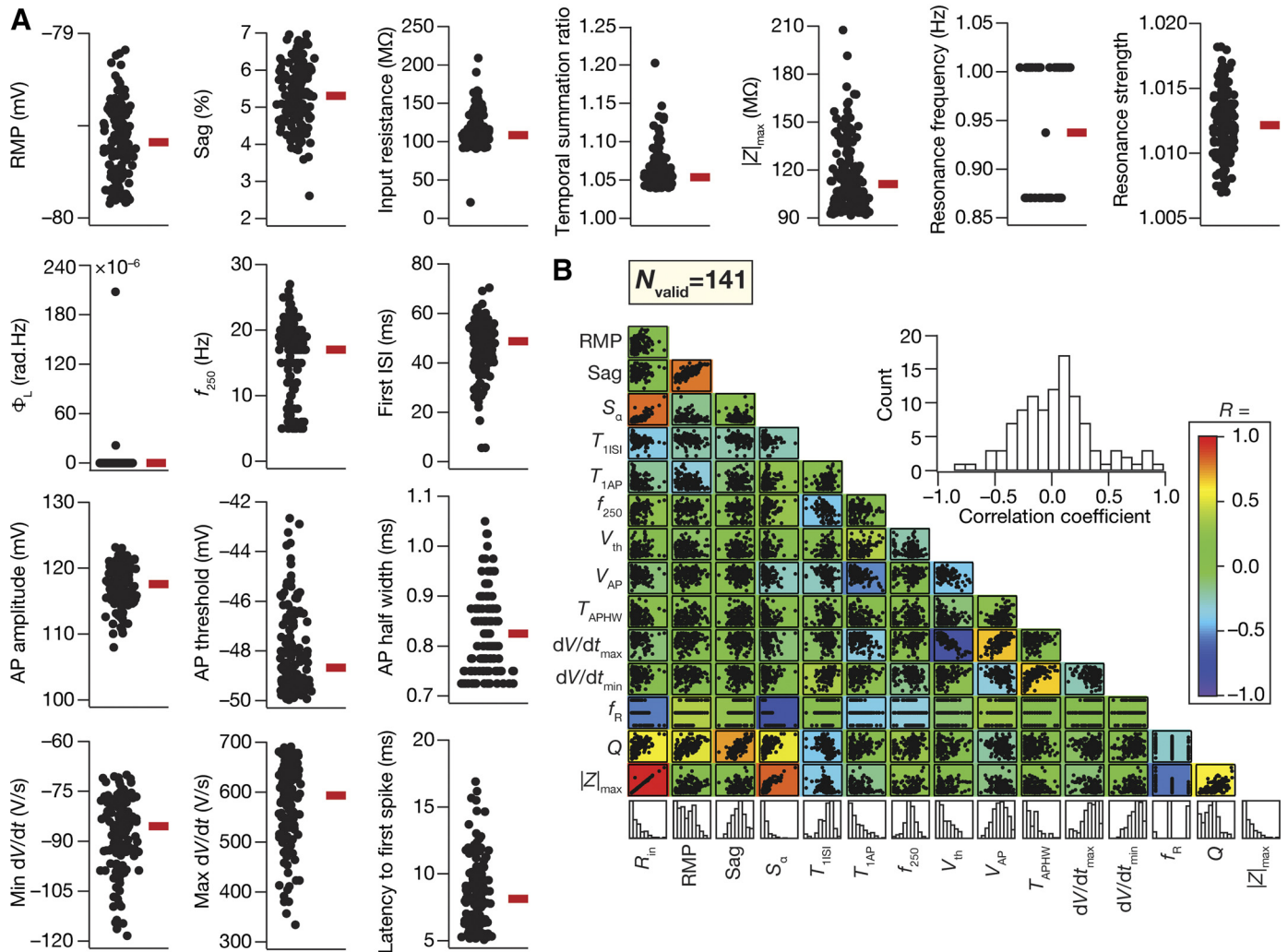
Figure 2. Heterogeneous distribution of characteristic physiological measurements in the valid granule cell models obtained by MPMOSS. *A*: Beeswarm plots depicting the distribution of eight subthreshold and eight suprathreshold measurements of the 141 valid models. The red rectangle adjacent to each plot depicts the respective median value. Of the 17 measurements used for validation, f_{50} for all valid models was identically zero by virtue of validation requirements (Table 2) and therefore is not shown. *B*: lower triangular matrix representing pair-wise correlations between 15 measurements underlying all valid models. Each box in the matrix depicts the scatter plot between the respective pair of measurements. The bottommost row represents the histograms of individual measurements in the valid model population. A heat map of Pearson's correlation coefficient (*R*) values corresponding to each scatter plot is superimposed on the matrix. *Inset*: histogram of the correlation coefficients spanning all pairs. Firing frequency at 50 pA (f_{50}) and total inductive phase (Φ_L) were not considered for the pairwise analysis as they were either identically zero for all models (f_{50}) or had very low values in a few models with the rest measured as zero (Φ_L).

dimensional manifold within the high-dimensional space (Fig. 3, *B–C*). Notwithstanding the absence of visible clusters, we performed automated clustering techniques on the coefficients associated with the dimensions computed with *t*-SNE (from Fig. 3*A*). We found three groups that occupied different subspaces within the 3-D *t*-SNE space (Fig. 3*A*). Importantly, these class labels, obtained from *t*-SNE coordinates, also showed grouping in the two other reduced dimensional spaces obtained with nonlinear techniques (Fig. 3, *B–C*), but not with PCA (Fig. 3*D*). Note that the group labels shown in Fig. 3 were derived from *t*-SNE coefficients and the same class labels are projected on other reduced dimensional spaces. We obtained similar results when we performed clustering analysis independently on PHATE, UMAP, and PCA dimensions and projected class labels onto the three other reduced dimensional spaces.

When we analyzed the measurements that were significantly different across three groups, we found six measurements (Fig. 3, *E–J*) that either showed minimal changes in overall distributions (Fig. 3, *E–G*) or manifested gradations within the valid (Tables 2 and 3) measurement range (Fig. 3, *H–J*). Importantly, the measurements that showed strong gradations (V_{AP}, V_{th}, and $dV/dt\,|_{max}$) were among the minority that showed strong dependencies across each other with the pair-wise correlation analysis (Fig. 2*B*). These results showed that these groups formed a smooth continuum along the different reduced dimensional spaces rather than manifesting spatially segregated clusters that are farther away from each other (Fig. 3).

Together, the lack of strong dependencies across most of the measurements (Figs. 2*B* and *3*) demonstrates that these measurements were quantifying disparate aspects of granule cell physiology. In summary, we found our model

population to be representative of the rat granule cell population because of the consistent relationship between our model population and experimental findings (2). The consistency of relationships was with reference to *1*) individual measurements (Fig. 2*A*); *2*) their pairwise codependencies (Fig. 2*B*); and *3*) the lack of strong structure in the reduced dimensional measurement space (Fig. 3).

Ion-Channel Degeneracy and Weak Parametric Cross-Dependencies in Valid Granule Cell Models

A small subset of random parametric combinations yielded valid granule cell models that satisfied all characteristic physiological properties. We analyzed the specific distributions of parameters and their cross-dependencies in these
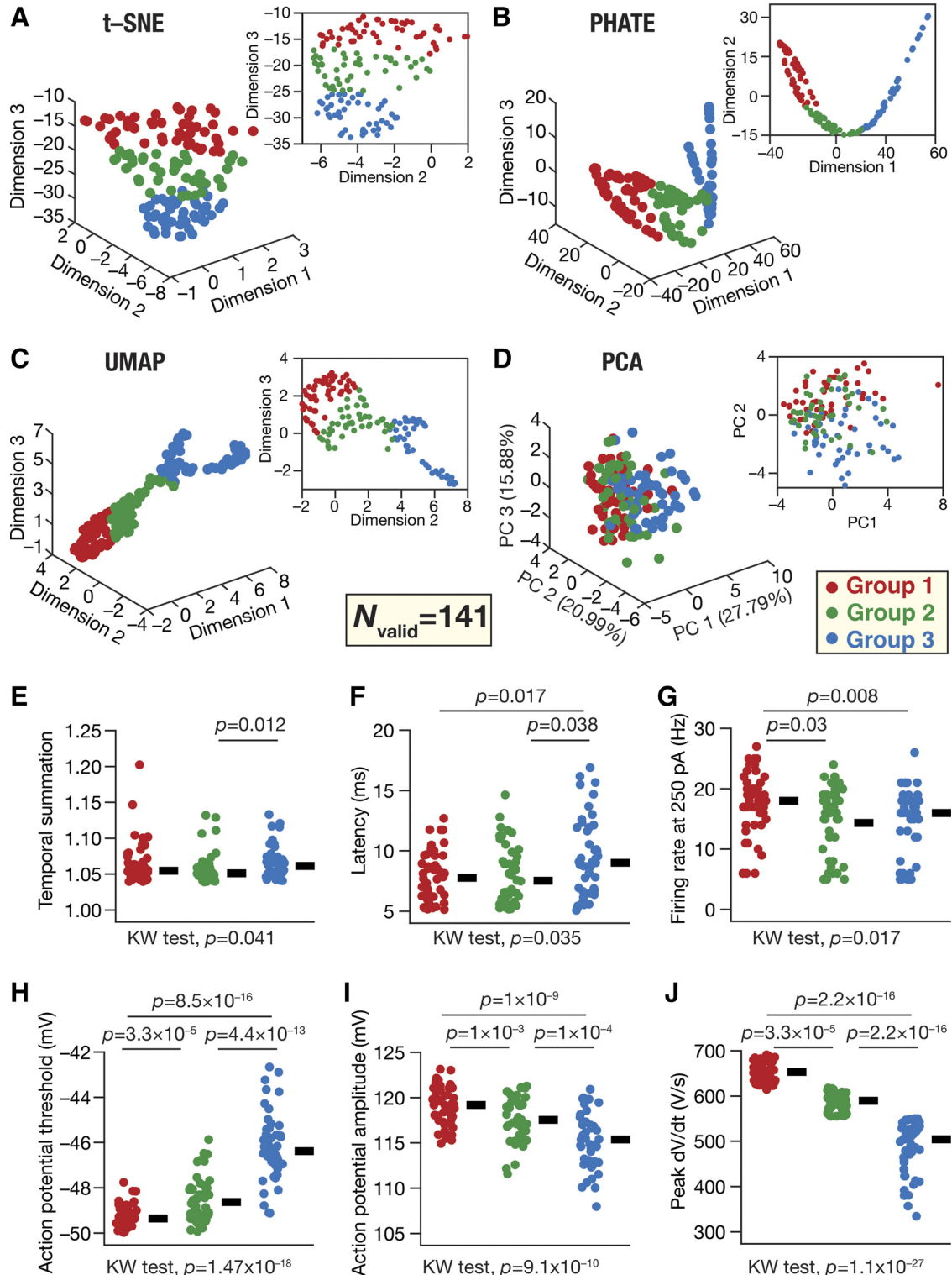
valid models. We noted that >99% random models did not satisfy all the 17 physiological constraints. This rules out one extreme of the randomness continuum, whereby any arbitrary set of random values assigned to these parameters would yield valid models. The other extreme is a scenario where there is a completely determined, single parametric combination that satisfies all physiological constraints, and all 141 valid models involve small shifts around that single parametric combination. To assess this scenario where all valid models are clustered around a single valid parametric combination, we first picked six of the 141 valid models that had very similar sub- (Fig. 4, A and B) and suprathreshold (Fig. 4C) physiological measurements. We plotted the 45 parameters associated with these functionally similar models spanning their respective min-max ranges from Table 1 (Fig. 4D). We found that the parameters associated with these six valid models spanned a large range of their min-max ranges (Fig. 4D). We looked at the distribution of each parameter across all 141 valid models that manifested characteristic GC physiology (Fig. 5). We found all of them to cover a wide span of their respective min-max ranges. Thus, there were several specific ion-channel combinations, with each parameter spanning a wide range that can satisfy all constraints associated with granule cell physiology. Together, these analyses rule out the other extreme of the randomness continuum, whereby all 141 models were clustered around a completely determined single parametric combination.

We assessed if the absence of clustering in the parametric space was because of strong parametric dependencies, where reduction in one parametric value was compensated in a pairwise manner by either an increase or decrease in the value of another parameter. Such pairwise relationships could occur if two different ion channels were functionally similar where one could be replaced by another without loss of function. In addition, there could be functions that require pairwise increase or decrease of specific pairs of ion channels, which could also be contributing to such pairwise relationships. A widespread prevalence of strong pairwise relationships would imply that the parametric space was not as high-dimensional as the numbers indicate but reduced to a low-dimensional space where highly cross-dependent parameters covary to yield valid models. To assess such pairwise relationships, we first computed Pearson's correlation coefficients (R) between each unique pair of parameters in the valid models. We found that none of the parametric pairwise correlations crossed an absolute value of 0.4, indicating very weak to weak correlations (85) between parameters of the valid models (Fig. 5). Thus, there were no strong pairwise relationships between parameters, indicating the absence of

strong pairwise cross-dependence in the parametric space. To further assess model separation in the parametric space, we computed pairwise distances between all 141 models using normalized Euclidean (Fig. 6A) and Mahalanobis (Fig. 6B) distance metrics. We found models to show large distances between themselves, with no models that were nearby in the parametric space (Fig. 6).

The absence of pairwise correlations ruled out strong pairwise dependencies (Fig. 5) and the distance analyses showed that the models were distant in the parametric space (Fig. 6). However, strong cross-dependencies involving several parameters could still yield an effectively low-dimensional space associated with valid model parameters. We asked if the parametric space associated with valid models was indeed high-dimensional or was mapped onto a low-dimensional space by applying nonlinear (Fig. 7, A–C) and linear (Fig. 7D) dimensionality reduction techniques on the parametric space. We found the variance explained by each of the first three principal components with PCA (Fig. 7D) to be minimal and a lack of strong clustering with any of the four dimensionality reduction techniques that we used (Fig. 7, A–D). Specifically, the reduced dimensional projections associated with nonlinear (Fig. 7, A–C) and linear (Fig. 7D) dimensionality reduction techniques did not visually manifest clusters. Similar to what we had observed with the measurement space (Fig. 3), some projections showed broad distributions spanning the reduced dimensional space (Fig. 7, A, C, and D), whereas others suggested the possibility of a low-dimensional manifold within the high-dimensional space (Fig. 7B).

We performed automated clustering techniques on the coefficients associated with the dimensions computed with t-SNE (from Fig. 7A). We found three groups that occupied different subspaces within the 3-D t-SNE space (Fig. 7A). Importantly, these class labels, obtained from t-SNE coordinates, also showed grouping in the two other reduced dimensional spaces obtained with nonlinear techniques (Fig. 7, B and C), but not with PCA (Fig. 7D). When we analyzed the parameters that were significantly different across three groups, we found seven parameters (Fig. 7, E–K) that either showed minimal changes in overall distributions (Fig. 7, F–K) or manifested gradations within their valid (Table 1) parametric range (Fig. 7E). The only parameter that showed gradation across the three groups was calcium decay constant (in all compartments except AIS) (Fig. 7E). We obtained similar results when we assigned group labels using the other dimensionality reduction techniques (PHATE, UMAP, and PCA) and projected class labels onto the three other reduced dimensional spaces. These results showed that these groups formed a smooth continuum

Figure 3. Linear and nonlinear dimensionality reduction analyses on the measurement space of the valid granule cell models. Outcomes of t-distributed stochastic neighbor embedding, t-SNE (A), potential of heat-diffusion for affinity-based trajectory embedding, PHATE (B), uniform manifold approximation and projection, UMAP (C), and principal component analysis, PCA (D) on the 15-dimensional measurement space of the 141 valid granule cell models. Firing frequency at 50 pA (f_{50}) and total inductive phase (Φ_L) were not considered for the pairwise analysis as they were either identically zero for all models (f_{50}) or had very low values in a few models with the rest measured as zero (Φ_L), thus yielding a 15-dimensional space of the 17 measurements for 141 (N_{valid}) valid models considered in Table 2 and Table 3. Insets in A–D show the projections of the data points along two dimensions. The three colors (red, blue, and green) in A–D correspond to the three groups obtained through k-means clustering analysis on t-SNE (in A) dimensions. Beeswarm plots of temporal summation (E), latency to first spike (F), firing rate at 250 pA (G), action potential threshold (H), action potential amplitude (I), and peak dV/dt (J) calculated from the first action potential elicited in response to a 250-pA current injection. These six measurements were found to be significantly different between the groups obtained using k-means clustering algorithm. The P values from Kruskal-Wallis test across the three groups and pairwise Wilcoxon rank-sum test are provided along with each plot. The other nine measurements (in the original 15-dimensional space) did not show significant differences across the three groups and are not plotted here.
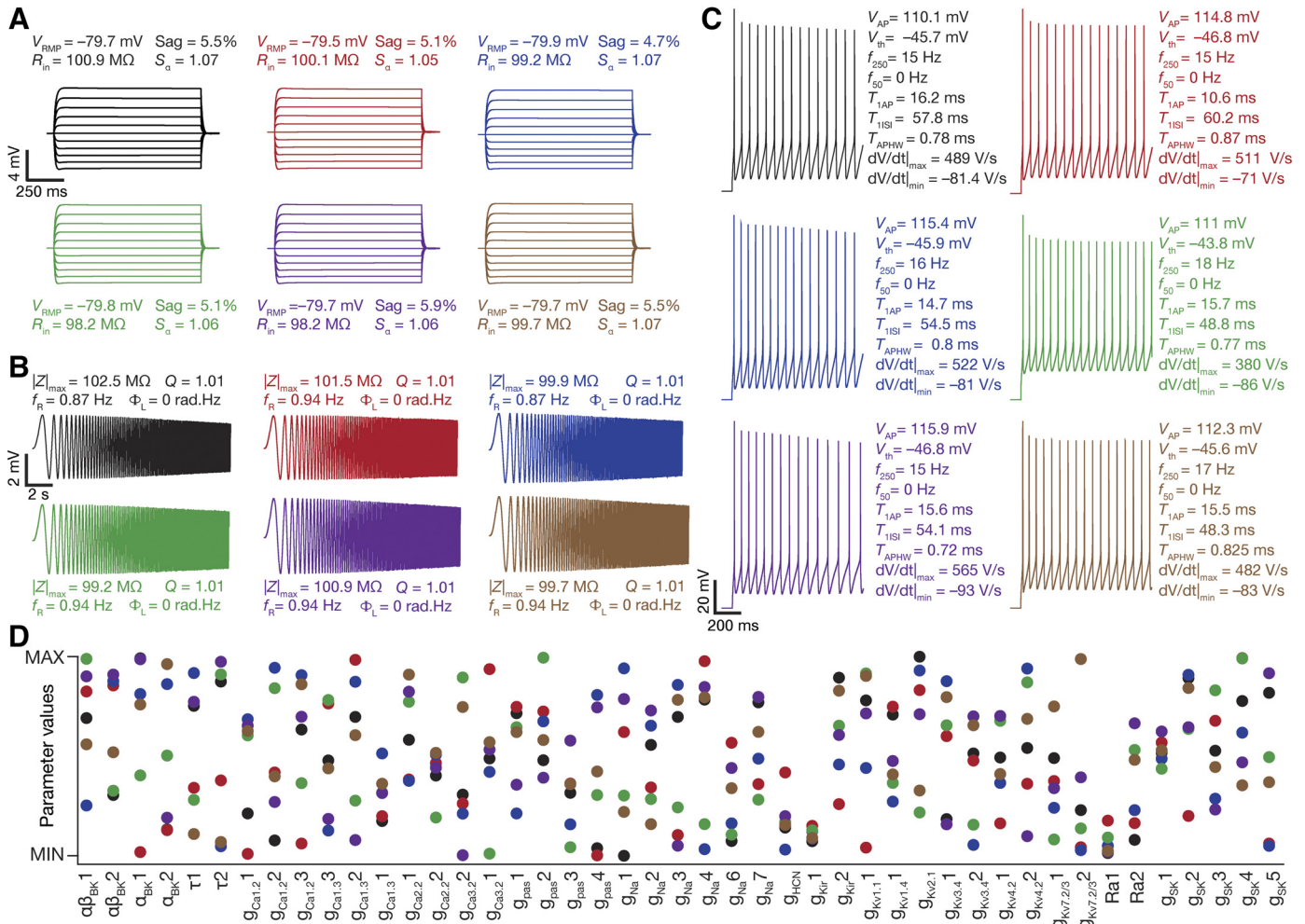
Figure 4. Disparate combinations of model parameters yielded similar physiological measurements in six randomly chosen valid granule cell models. *A*: voltage responses of six different valid models with similar measurements for current injections spanning from −50 to +50 pA in steps of 10 pA. *B*: voltage responses of the six functionally similar models to chirp current injection. *C*: voltage responses of the six models to a 250-pA depolarizing current injection showing action potential firing. All 17 measurements for the six similar models are depicted across *A–C*. *D*: normalized values of the 45 parameters that defined each valid GC model, shown for the six functionally similar models whose measurements are depicted in *A–C*. Normalization was with reference to the respective minimum and maximum bounds for that parameter (Table 1). Distinct colors uniquely identify different models across all panels.

along the different reduced dimensional spaces rather than manifesting spatially segregated clusters that are farther away from each other (Fig. 7).

Finally, we projected these parametric group labels (from Fig. 7) to the measurement space (in Fig. 3, across all 4 dimensionality reduction techniques) to ask if these parametric groups translated to grouping of measurements. We found overlapping group labels in the measurement space, implying the absence of grouping in the measurement space driven by grouping in the parametric space. Similar results were obtained when we used group labels from the measurement space (from Fig. 3) to identify potential grouping in the parametric space (in Fig. 7, across all 4 dimensionality reduction techniques). These results together demonstrated that grouping in the parametric space did not yield grouping in measurement space and vice versa, together confirming degeneracy and pleiotropy in the mapping between the parametric and measurement spaces (12, 86, 87).

Together, the absence of strong pairwise correlations (Fig. 5), the large distance between models in the parametric space (Fig. 6), and the lack of well-defined clustering in low-dimensional spaces (Fig. 7) ensure the high-dimensional nature of the parametric space and rule out strong cross-dependencies across different model parameters.

Heterogeneities in Propagation Physiology of Valid Granule Cell Models

Did all valid granule cell models manifest similar information transfer characteristics across the somatodendritic arbor? We analyzed synaptic information transfer by studying unitary activation of synapses located at each of the several dendritic locations in the GC morphology (Fig. 8A). In the base model, we activated a single synapse containing AMPA receptors at a selected dendritic location, adjusting the receptor density such that the propagated somatic EPSP was in the 0.2–0.3 mV range to match with electrophysiological recordings from granule cells (63). We measured the
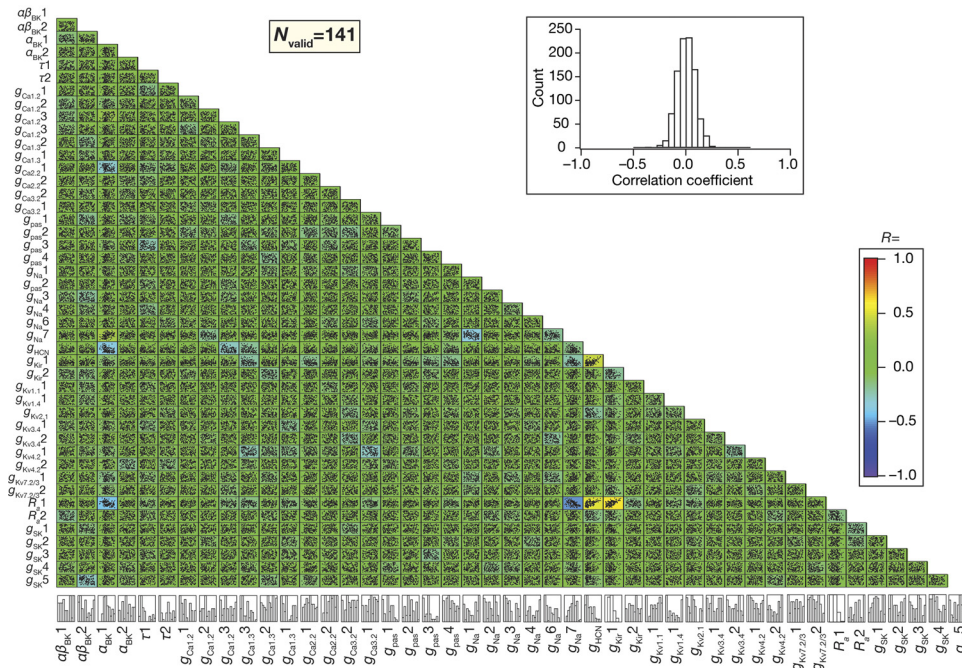
Figure 5. Weak pairwise correlations between parameters that defined the valid granule cell model population. Lower triangular matrix representing correlation between the values of the 45 parameters that defined the 141 valid models ($N_{valid} = 141$). Each box in the matrix depicts the scatter plot between respective parameter pairs. The bottommost row represents the histograms for individual parameters in the valid model population. A heat map of Pearson's correlation coefficient values corresponding to each scatter plot is superimposed on the matrix. *Inset*: histogram of the correlation coefficients spanning all pairs.

local dendritic voltage at the location of the synapse and the propagated somatic voltage for this location (Fig. 8B). We repeated this for all dendritic locations (Fig. 8C). As expected, we found that with increasing path distance of the synaptic location from the soma, there was an increase in the local dendritic voltage required to maintain the somatic EPSP within the 0.2–0.3 mV range (Fig. 8C). At the end of this procedure in the base model, we had a value for the AMPAR density that met the target somatic voltage requirement for each location across the dendritic arborization. We used these location-dependent receptor density values (obtained from the base model) to assess heterogeneities of propagation across the 141 valid GC models. Specifically, if all valid models behaved the same as the base model, then the somatic EPSP amplitude will be in the 0.2–0.3 mV for

all valid models, irrespective of synaptic location. A deviation from this range would indicate heterogeneities in synaptic information transfer across valid models.

We found pronounced heterogeneities in synaptic information transfer across different valid models. Three illustrative examples are shown in Fig. 8, D–E, demonstrating wide variability in local dendritic synaptic responses as well as in propagated somatic voltages, for an identical synapse at the same location across models. Although the dendritic voltage responses were larger with increased synaptic distance from the soma (Fig. 8D), there were differences across models in the magnitude of this increase as well as in how they propagated to the soma. These are consequent to differences in active dendritic components of the different models. Importantly, when we assessed local dendritic (Fig. 8, F and
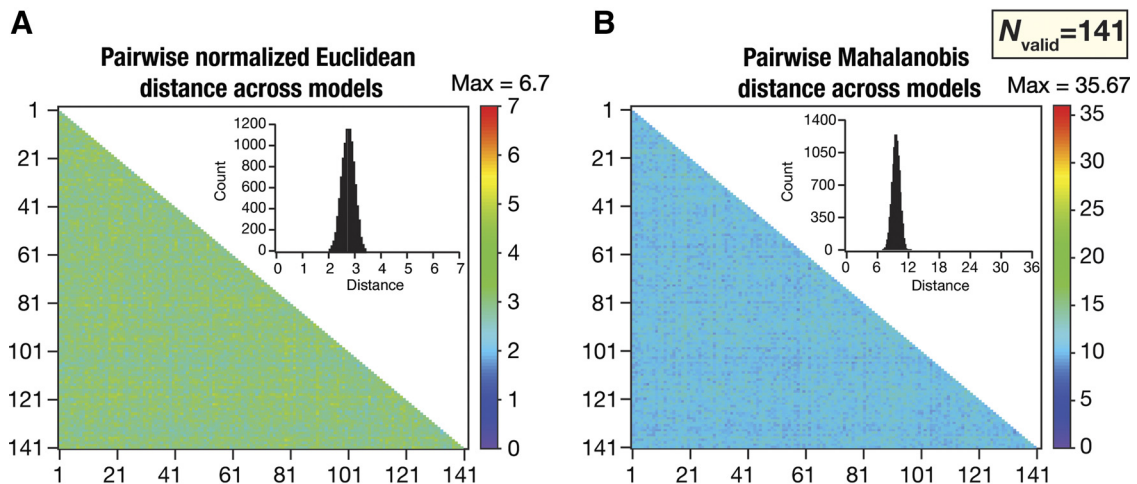
Figure 6. Large pairwise distances between parameters that defined the valid granule cell model population. Heterogeneities in model parameters were quantified with normalized Euclidean (*A*) and Mahalanobis (*B*) distance metrics. The matrices represent the pairwise distance between the parametric vectors defining each of the 141 valid models ($N_{valid} = 141$). *Insets* show the histogram of all values in the respective distance matrix.

G) and somatic (Fig. 8*G*) voltages across all somatodendritic locations in all 141 valid models, we found their ranges to be consistent with their experimental counterparts (63). Specifically, the somatic unitary EPSP was predominantly in the 0.1–0.4 mV range, with a dominant proportion falling within the 0.2–0.3 mV. The local dendritic voltage was in the

0.2–0.9 mV for proximal dendritic locations and in the 0.5–9 mV range for distal dendritic locations (Fig. 8*G*), which match with the ranges reported from electrophysiological recordings (63). Although synaptic information transfer was not used as a validation criterion for model generation, we found the dendritic unitary synaptic responses and the
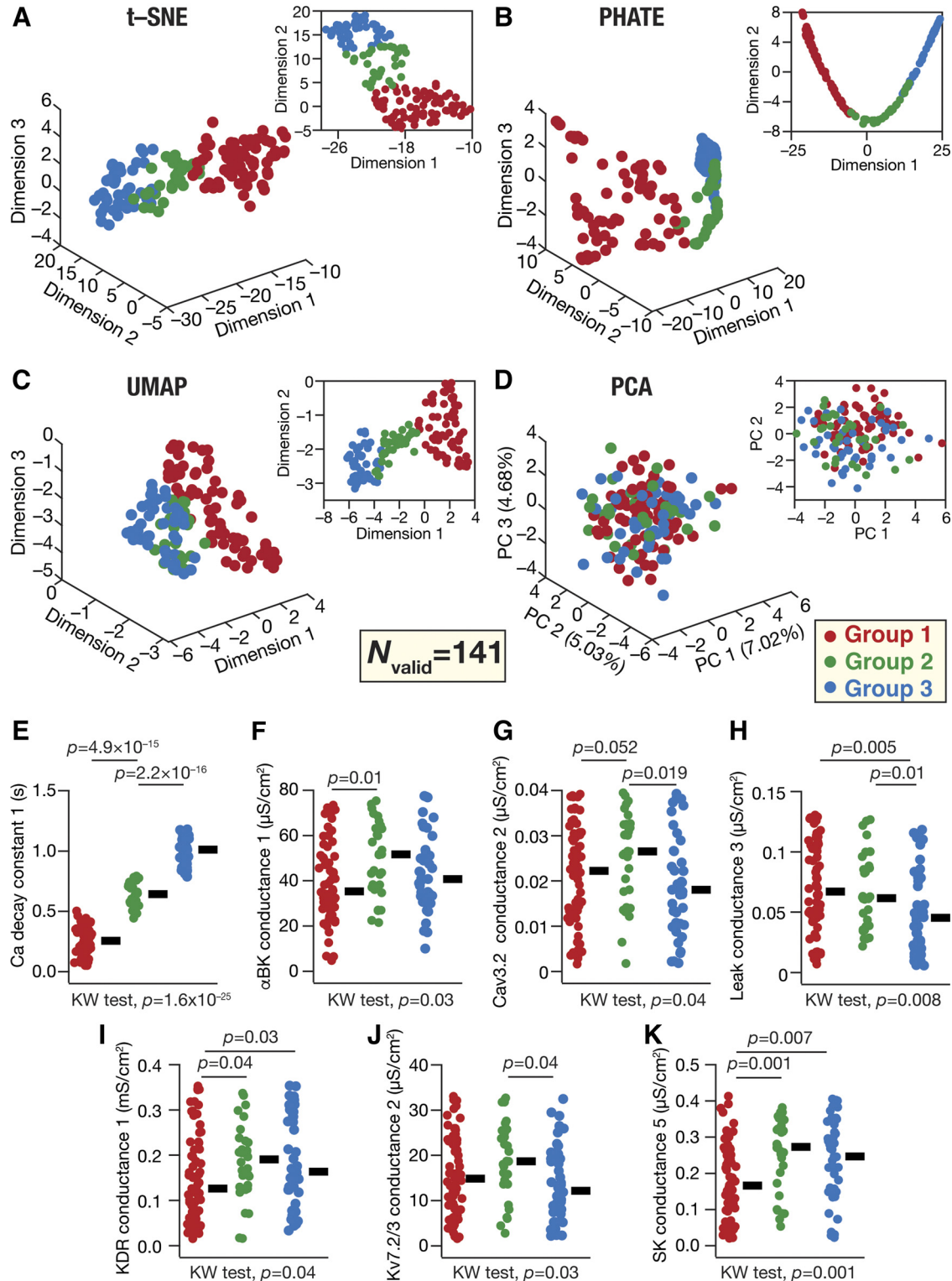
propagated somatic voltages to match with their respective distributions across rat granule cells.

We assessed backpropagation of action potentials by initiating a single action potential at the cell body and recording the action potential at all somatodendritic locations. We repeated this for all 141 valid models to assess heterogeneities in action potential backpropagation. We found pronounced heterogeneities in the profile of backpropagation. Although some models sustained large-amplitude backpropagating action potentials, others manifested considerable attenuation (Fig. 9, *A–D*). The overall reduction in the amplitude of dendritic action potentials (Fig. 9, *D* and *E*) and heterogeneities therein (Fig. 9) were comparable with electrophysiological ranges reported for DG granule cells (63). Thus, although backpropagating action potentials were not explicitly constrained in the validation process of these models, we found these models to match electrophysiological counterparts in action potential backpropagation and associated heterogeneities across models.

DISCUSSION

Our study involved three-dimensional, morphologically realistic models of the dentate gyrus granule cell that were constrained by the set of ion channels that they express and several electrophysiological measurements that characterize their cellular neurophysiology. We used a computationally complex stochastic search algorithm spanning all biophysical parameters that defined the model to search for valid granule cell models. A small subset of valid model, among thousands of randomly generated models, satisfied several sub- and suprathreshold electrophysiological measurements that were obtained from dentate gyrus granule cells (2). Somatodendritic measurements from this valid model population were heterogeneous and matched with their electrophysiological counterparts. The different electrophysiological measurements used to identify valid models quantified different aspects of granule cell physiology and matched pairwise dependencies of their electrophysiological counterparts (2). Importantly, the valid model parameters were neither arbitrarily random nor clustered around a single parametric combination and showed weak cross-dependencies in the parametric space. These observations are consistent with a system that manifests a high degree of complexity, involving specific combinations of disparate ion-channel contributions toward achieving characteristic granule cell physiology. In addition, consistent with complex systems, the emergence of granule cell characteristic physiology showed degeneracy (28). Specifically, disparate combinations of functionally specialized subsystems (ion channels and other biophysical systems) yielded similar functional outcomes in the integrated complex system (the granule cell), resulting in the coexistence of functional specialization and functional integration within the complex system (28, 87–89).

Heterogeneities and Degeneracy in Neuronal Physiology

Biological complex systems manifest pronounced heterogeneities and exhibit degeneracy in the realization of precise functional outcomes. The nervous system in general, and the mammalian hippocampal formation with specific reference to this study, is no exception to this observation (11, 12, 14, 88–96). Within the mammalian hippocampal formation, degeneracy in the emergence of characteristic physiological properties has been observed in pyramidal neurons of the CA1 (16, 17, 20, 68, 73, 74, 97), pyramidal neurons of the CA3 (21), basket (1) and granule (1, 3–5, 8) cells of the dentate gyrus, and stellate cells of the entorhinal cortex (18, 19). In addition, with reference to encoding functions of the hippocampal formation, degeneracy has been demonstrated in the emergence of short- (72) and long-term plasticity profiles in CA1 (70, 98) and DG (71), network decorrelation in the DG (1, 3), place-cell tuning profiles in CA1 (25–27), spatial information transfer of CA1 place cells with rate (25) or phase (75) coding, and in spatial coding functions of the dorsoventral entorhinal axis (99). The ubiquitous nature of degeneracy in neural systems is emphasized by the several outstanding reviews on degeneracy, spanning different scales and different species (11, 12, 28, 87, 90, 91, 93, 94, 96, 100–108).

In this study, our results extend previous lines of evidence for the manifestation of degeneracy in the emergence of characteristic physiological properties of DG granule cells (1, 3–5, 8). Our extension involved an extensive search of morphologically realistic granule cell models and covered a wide set of electrophysiological measurements that were all measured from the same set of biological granule cells (2). This set of biological measurements allowed us to not only look at the distributions of individual measurements but also ask if there were second- and higher-order relationships between model measurements and if they were comparable to experimental observations. We find the distributions and the codependencies of individual measurements to be comparable to their experimental counterparts (Figs. 2 and 3), thus providing a valid population of granule models that match with their biological counterparts.

Propagation measurements (both forward propagation of synaptic potentials and backpropagation of action potentials) in our models were also heterogeneous, with their somatic and dendritic distributions matching with their respective electrophysiological counterparts (Figs. 8 and 9). Based on analyses from other neurons within the hippocampal formation (11, 31, 32, 109–118), local synaptic responses and signal

Figure 7. Linear and nonlinear dimensionality reduction analyses on the parameter space of the valid granule cell models. Outcomes of *t*-distributed stochastic neighbor embedding, *t*-SNE (*A*), potential of heat-diffusion for affinity-based trajectory embedding, PHATE (*B*), uniform manifold approximation and projection, UMAP (*C*), and principal component analysis, PCA (*D*) on the 45-dimensional parametric space (Table 1) of the 141 valid ($N_{\text{valid}} = 141$) granule cell models. *Insets* in *A–D* show the projections of the data points along two dimensions. The three colors (red, blue, and green) in *A–D* correspond to the three groups obtained through *k*-means clustering analysis on *t*-SNE (in *A*) dimensions. Beeswarm plots of Ca decay constant (*E*), αBK conductance (*F*), Cav3.2 conductance (*G*), leak conductance (*H*), delayed rectifier potassium conductance (*I*), Kv7.2/3 conductance (*J*), and SK conductance (*K*). The numbers provided in the parameter values specify their locations within the neuronal arbor (Table 1). These seven parameters were found to be significantly different between the groups obtained using *k*-means clustering algorithm. The *P* values from Kruskal-Wallis test across the three groups and pairwise Wilcoxon rank-sum test are provided along with each plot. The other 38 parameters (in the original 45-dimensional parametric space) did not show significant differences across the three groups and are not plotted here.
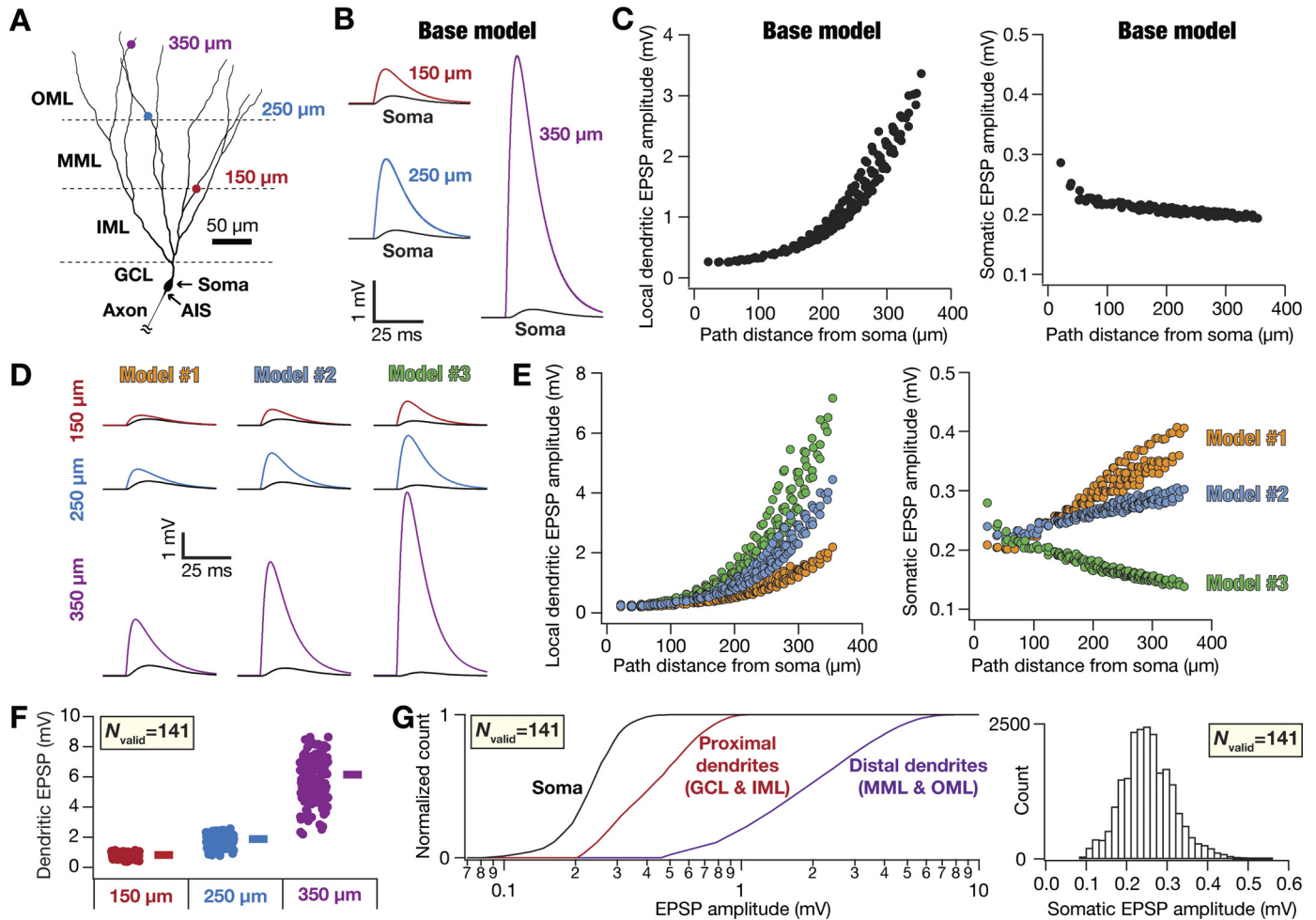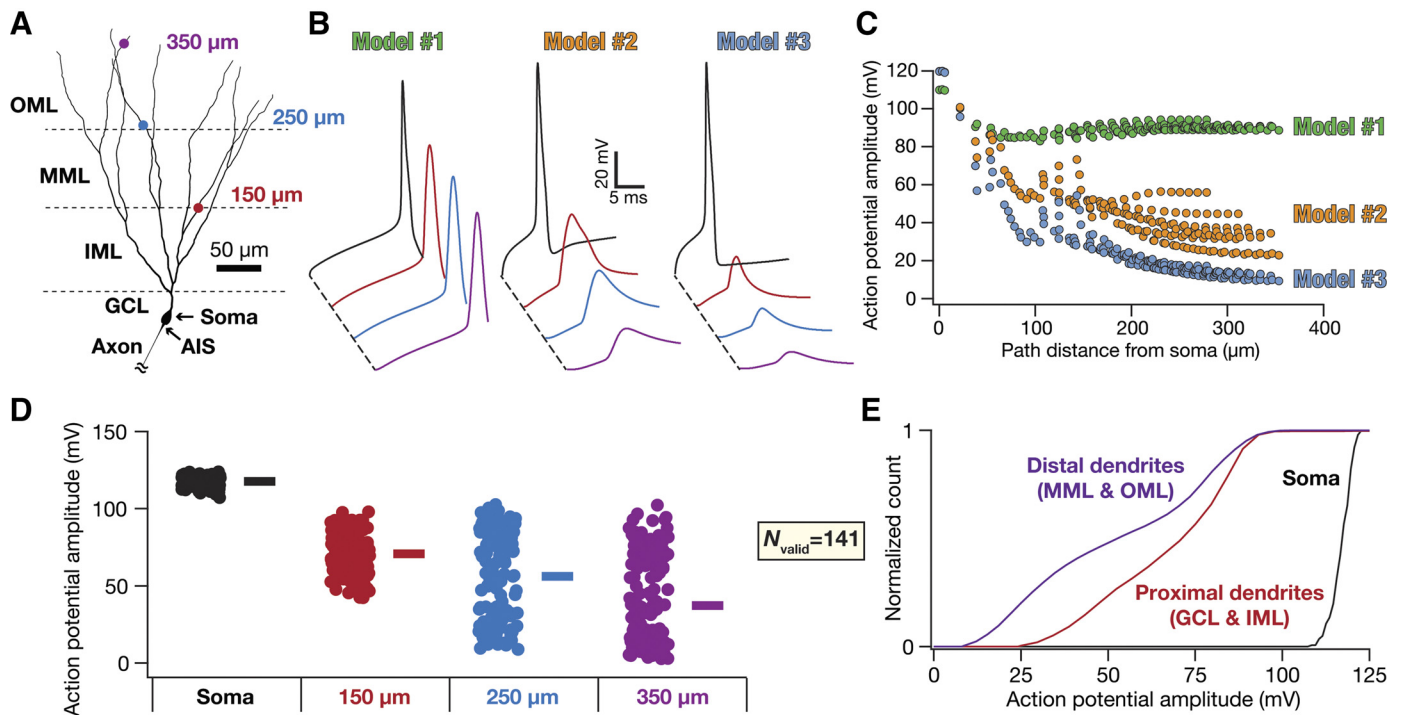
Figure 8. Heterogeneities in forward synaptic propagation across the somatodendritic arbor of valid granule cell models. *A*: two-dimensional projection of the 3-D morphology of DG granule cell showing the four locations (Soma, 150 μm, 250 μm, and 350 μm) where illustrative examples of heterogeneities are shown. The numbers represent path distances of marked dendritic locations from the soma. *B*: excitatory postsynaptic potentials (EPSPs) generated by the activation of single synapses located at each of the three dendritic locations shown in *A*. The local dendritic voltage trace at the specified synaptic location (colored traces) and the propagated somatic voltage trace (black) are plotted for each of the three dendritic locations on the base model. *C*: local dendritic EPSP amplitude (*left*) and the propagated somatic counterpart (*right*), computed for all somatodendritic compartments, plotted against the location of the single synapse on the base model. It may be noted that the somatic voltage was in the 0.2–0.3 mV range irrespective of synaptic location (*right*). The local dendritic voltage required to retain somatic voltage at 0.2–0.3 mV increased with increase in distance from the soma (*left*). *D*: local dendritic EPSP traces and the propagated somatic counterpart (black) for the three synaptic locations (from *A*), shown for three different valid models. *E*: local dendritic EPSP amplitude (*left*) and the propagated somatic counterpart (*right*), computed for all somatodendritic compartments, plotted against the location of the single synapse for the three valid models illustrated in *D*. The heterogeneities in the recorded amplitudes might be noticed across the three models, as well as with reference to the base model (*C*) *F*: local dendritic EPSP amplitude recorded at the three dendritic locations marked in *A* for all 141 valid models. Colored bars beside each plot represent the respective median of the distribution. *G*, *left*: cumulative histograms of somatic and local dendritic EPSP amplitude recorded for all somatodendritic locations for all 141 valid models (N_{valid} = 141). Histograms are shown for somatic, proximal dendritic (encompassing GCL and IML), and distal dendritic (locations in MML and OML) locations. *Right*: histogram of somatic EPSP amplitude associated with all somatodendritic locations for all 141 valid models. For *D–F*, the AMPAR density of synapses across all valid models was taken from the base model for each synaptic location (*C*). GCL, granule cell layer; IML, inner molecular layer; MML, middle molecular layer; OML, outer molecular layer.

propagation across the dendritic arbor are known to be dependent on morphological characteristics, passive cable properties, active dendritic conductances, and other neuronal components (e.g., intracellular stores, buffers). Future electrophysiological and computational studies in DG granule cells should explore the role of these different components in mediating heterogeneities in local and transfer impedances, synaptic responses across somatodendritic locations, and action potential backpropagation.

Our analyses demonstrate that these characteristic granule cell models emerge with their distributions spanning a wide range of parametric combinations with weak cross-dependencies in the parametric space (Figs. 5 and 6). These observations translate to expansive degrees of freedom available to DG granule cells toward achieving characteristic physiological properties despite morphological and ion-channel distribution constraints. A fundamental advantage for the expression of degeneracy in biological system is the ability to achieve robust function through several disparate routes, thus reducing dependencies on any single component for executing precise function.

Figure 9. Heterogeneities in backpropagation of action potentials across the somatodendritic arbor of valid granule cell models. *A*: two-dimensional projection of the 3-D morphology of DG granule cell showing the four locations (Soma, 150 µm, 250 µm, 350 µm) where illustrative examples of heterogeneities are shown. The numbers represent path distances of marked dendritic locations from the soma. *B*: propagating action potential traces of three different valid models at the four locations marked in *A*. *C*: action potential amplitude recorded at all somatodendritic locations for the three valid models illustrated in *B*. *D*: action potential amplitude recorded at the four locations marked in *A* for all 141 valid models (N_{valid} = 141). Colored bars beside each plot represent the respective median of the distribution. *E*: cumulative histograms of action potential amplitude recorded at all somatodendritic locations for all 141 valid models. Histograms are shown for somatic, proximal dendritic (encompassing GCL and IML), and distal dendritic (locations in MML and OML) locations. GCL, granule cell layer; IML, inner molecular layer; MML, middle molecular layer; OML, outer molecular layer.

These distinctions in the specific route taken to achieve characteristic functions might also translate to effective implementation of certain functions (3, 4) or heterogeneities in other aspects (71) of granule cell physiology that account for the three-dimensional morphology. Specifically, the presence of multiple routes to achieve signature physiological characteristics ensures that there is no need for maintaining individual channel densities at specific values toward achieving precise function. Degeneracy provides a substrate for achieving *1*) robustness of functional outcomes despite the presence of widespread heterogeneities in the morphological properties and ion-channel distributions (21, 25–27, 119–121) and *2*) resilience in the face of targeted perturbations to specific components, because resilience could be achieved through several routes that do not involve the components that were targeted by the perturbations (22, 73, 74, 90, 108, 122–124). In addition, the heterogeneities in components that yielded robustness and resilience in one set of functions could yield heterogeneities in other functions. For instance, there could be scenarios where the physiological properties are comparable, but the plasticity profiles are heterogeneous; conversely, similar plasticity profiles could be achieved with very different structural and biophysical components (70, 71).

There are strong lines of evidence for a many-to-many mapping between ion channels and specific physiological characteristics in DG granule cells. Specifically, there are different lines of computational (3, 5, 8) and electrophysiological/pharmacological (4) lines of evidence from DG granule cells that the relationship between channels and measurements is many-to-many, manifesting both degeneracy and pleiotropy. These results emphasize the need to account for the global structure of the parametric space rather than focusing on one-to-one relationships involving individual components and their impact on specific measurements (4, 8, 11, 12, 14, 33, 74, 86, 87, 90, 125).

Future Directions

The demonstration of degeneracy in morphologically realistic granule cell models, strongly constrained by several functional measurements and their codependencies, is a first step in understanding the physiology and pathophysiology of DG granule cells, their dendritic physiology, and network interactions. There are several specific directions that could be pursued with the understanding that the emergence of their physiology manifests degeneracy and that they form a complex system where functional specialization coexists with functional integration. First, there are differences in the morphology, physiology, and biophysical composition of DG granule cells in different locations and different states. These differences are known to exist along the dorsoventral axis of the hippocampus (126–134), pathological conditions (52, 135–144), and uniquely for DG granule cells, adult neurogenesis (5, 9, 145–154). The overall approach used here could be used to build different heterogeneous populations of granule cells built with distinct morphologies and disparate sets of ion

channels that emerge from respective experimental measurements that span a large set of characteristics from the same set of cells. Such analyses would enable a fundamental understanding of differences in heterogeneities, composition, extent of degeneracy in each state, and how they contribute to the physiology of the neurons and their networks (12, 86, 90, 92, 96, 104, 155–157).

Such insights about individual neuronal physiology and their composition could then be used to assess network scale functions such as different forms of decorrelation (1, 3, 4, 128, 158–169) and engram cell formation (71, 92, 170–178) assessed with morphologically realistic heterogeneous model populations of different neuronal subtypes in the hippocampus. The use of heterogeneous morphologically realistic models for all neuronal subtypes would provide deeper insights into degeneracy in the emergence of DG network function (1, 3) and the role of active dendrites in mediating decorrelation as well as engram cell formation (169, 179).

An essential requirement in the design and implementation of morphologically realistic models is biophysical and physiological data from the dendrites of DG neurons. Dendrites in CA1 neurons have been thoroughly studied from the perspective of biophysical and physiological characterization, including thorough pharmacological analyses of dendritic measurements across distance (65, 66, 97, 109, 113, 180–184). The richness of the data has resulted in strongly constrained models probing different aspects of degeneracy in CA1 pyramidal neurons, including the analyses of dendritic physiology and biophysics (11, 16, 17, 20, 25–27, 68, 70, 72, 75, 185). In striking contrast, there is a paucity of data on dendritic biophysics, physiology, plasticity, and pharmacology for DG neurons, resulting in minimal set of dendritic measurements that can be strongly constrained in a model (63). Therefore, there is an urgent need for data, using cell-attached and current-clamp recordings coupled with pharmacology targeting different channels, on dendrites of DG neurons. The availability of such data could then translate to strongly constrained morphologically realistic models that can thoroughly explore the manifestation of degeneracy in the ionic basis of dendritic physiology in these neurons. As a vast majority of information processing in a neuron happens in their active dendrites, it is essential that data on the biophysical composition and the pharmacological profile of physiological measurements of dendrites are rigorously characterized. Future modeling studies should therefore be strongly coupled with electrophysiological, biophysical, and pharmacological characterization of DG neuronal dendrites.

Finally, the use of such network models with strongly constrained morphologically realistic neurons that manifest degeneracy at different scales could be used to assess the multifarious and heterogeneous impact of different neuromodulators across different cells at different locations. In addition to changes mediated by neuromodulation, such morphologically realistic model populations could also be used to assess plasticity profile degeneracy (70, 71), plasticity heterogeneities (71), and plasticity degeneracy (22) in implementing the encoding functions of the DG network.

DATA AVAILABILITY

This is a computational study and therefore no experimental data were generated as part of this study. All computational outcomes and analyses required for assessment of this manuscript are available as part of the figures and tables. The source codes used for simulations are publicly available at https://doi.org/10.5281/zenodo.13309600.

DISCLOSURES

No conflicts of interest, financial or otherwise, are declared by the authors.

AUTHOR CONTRIBUTIONS

S.K. and R.N. conceived and designed research; S.K. performed experiments; S.K. analyzed data; S.K. and R.N. interpreted results of experiments; S.K. prepared figures; S.K. and R.N. drafted manuscript; S.K. and R.N. edited and revised manuscript; S.K. and R.N. approved final version of manuscript.

REFERENCES

1. **Mishra P**, **Narayanan R.** Disparate forms of heterogeneities and interactions among them drive channel decorrelation in the dentate gyrus: degeneracy and dominance. *Hippocampus* 29: 378–403, 2019. doi:10.1002/hipo.23035.

2. **Mishra P**, **Narayanan R.** Heterogeneities in intrinsic excitability and frequency-dependent response properties of granule cells across the blades of the rat dentate gyrus. *J Neurophysiol* 123: 755–772, 2020. doi:10.1152/jn.00443.2019.

3. **Mishra P**, **Narayanan R.** Ion-channel regulation of response decorrelation in a heterogeneous multi-scale model of the dentate gyrus. *Curr Res Neurobiol* 2: 100007, 2021. doi:10.1016/j.crneur.2021.100007.

4. **Mishra P**, **Narayanan R.** Ion-channel degeneracy: multiple ion channels heterogeneously regulate intrinsic physiology of rat hippocampal granule cells. *Physiol Rep* 9: e14963, 2021. doi:10.14814/phy2.14963.

5. **Beining M**, **Mongiat LA**, **Schwarzacher SW**, **Cuntz H**, **Jedlicka P.** T2N as a new tool for robust electrophysiological modeling demonstrated for mature and adult-born dentate granule cells. *eLife* 6: e26517, 2017. doi:10.7554/eLife.26517.

6. **Zhang X**, **Jonas P.** Integration of spatial and non-spatial information by heterogeneous dentate gyrus granule cells. *J Life Sci (Westlake Village)* 2: 19–24, 2020.

7. **Zhang X**, **Schlögl A**, **Jonas P.** Selective routing of spatial information flow from input to output in hippocampal granule cells. *Neuron* 107: 1212–1225.e1217, 2020. doi:10.1016/j.neuron.2020.07.006.

8. **Schneider M**, **Bird AD**, **Gidon A**, **Triesch J**, **Jedlicka P**, **Cuntz H.** Biological complexity facilitates tuning of the neuronal parameter space. *PLoS Comput Biol* 19: e1011212, 2023. doi:10.1371/journal.pcbi.1011212.

9. **Huckleberry KA**, **Shansky RM.** The unique plasticity of hippocampal adult-born neurons: contributing to a heterogeneous dentate. *Hippocampus* 31: 543–556, 2021. doi:10.1002/hipo.23318.

10. **Marder E**, **Taylor AL.** Multiple models to capture the variability in biological neurons and networks. *Nat Neurosci* 14: 133–138, 2011. doi:10.1038/nn.2735.

11. **Rathour RK**, **Narayanan R.** Degeneracy in hippocampal physiology and plasticity. *Hippocampus* 29: 980–1022, 2019. doi:10.1002/hipo.23139.

12. **Goaillard JM**, **Marder E.** Ion channel degeneracy, variability, and covariation in neuron and circuit resilience. *Annu Rev Neurosci* 44: 335–357, 2021. doi:10.1146/annurev-neuro-092920-121538.

13. **Foster WR**, **Ungar LH**, **Schwaber JS.** Significance of conductances in Hodgkin-Huxley models. *J Neurophysiol* 70: 2502–2518, 1993. doi:10.1152/jn.1993.70.6.2502.

14. **Goldman MS**, **Golowasch J**, **Marder E**, **Abbott LF.** Global structure, robustness, and modulation of neuronal models. *J Neurosci* 21: 5229–5238, 2001. doi:10.1523/JNEUROSCI.21-14-05229.2001.

15. **Prinz AA**, **Billimoria CP**, **Marder E.** Alternative to hand-tuning conductance-based models: construction and analysis of databases of model neurons. *J Neurophysiol* 90: 3998–4015, 2003. doi:10.1152/jn.00641.2003.

16. **Rathour RK**, **Narayanan R.** Inactivating ion channels augment robustness of subthreshold intrinsic response dynamics to parametric variability in hippocampal model neurons. *J Physiol* 590: 5629–5652, 2012. doi:10.1113/jphysiol.2012.239418.

17. **Rathour RK**, **Narayanan R.** Homeostasis of functional maps in active dendrites emerges in the absence of individual channelostasis. *Proc Natl Acad Sci USA* 111: E1787–E1796, 2014. doi:10.1073/pnas.1316599111.

18. **Mittal D**, **Narayanan R.** Degeneracy in the robust expression of spectral selectivity, subthreshold oscillations and intrinsic excitability of entorhinal stellate cells. *J Neurophysiol* 120: 576–600, 2018. doi:10.1152/jn.00136.2018.

19. **Mittal D**, **Narayanan R.** Heterogeneous stochastic bifurcations explain intrinsic oscillatory patterns in entorhinal cortical stellate cells. *Proc Natl Acad Sci USA* 119: e2202962119, 2022. doi:10.1073/pnas.2202962119.

20. **Migliore R**, **Lupascu CA**, **Bologna LL**, **Romani A**, **Courcol JD**, **Antonel S**, **Van Geit WAH**, **Thomson AM**, **Mercer A**, **Lange S**, **Falck J**, **Rössert CA**, **Shi Y**, **Hagens O**, **Pezzoli M**, **Freund TF**, **Kali S**, **Muller EB**, **Schürmann F**, **Markram H**, **Migliore M.** The physiological variability of channel density in hippocampal CA1 pyramidal cells and interneurons explored using a unified data-driven modeling workflow. *PLoS Comput Biol* 14: e1006423, 2018. doi:10.1371/journal.pcbi.1006423.

21. **Roy R**, **Narayanan R.** Ion-channel degeneracy and heterogeneities in the emergence of complex spike bursts in CA3 pyramidal neurons. *J Physiol* 601: 3297–3328, 2023. doi:10.1113/JP283539.

22. **Nagaraj H**, **Narayanan R.** Plasticity manifolds and degeneracy govern circadian oscillations of neuronal intrinsic properties in the suprachiasmatic nucleus. *iScience* 26: 106503, 2023. doi:10.1016/j.isci.2023.106503.

23. **Arnaudon A**, **Reva M**, **Zbili M**, **Markram H**, **Van Geit W**, **Kanari L.** Controlling morpho-electrophysiological variability of neurons with detailed biophysical models. *iScience* 26: 108222, 2023. doi:10.1016/j.isci.2023.108222.

24. **Reva M**, **Rössert C**, **Arnaudon A**, **Damart T**, **Mandge D**, **Tuncel A**, **Ramaswamy S**, **Markram H**, **Van Geit W.** A universal workflow for creation, validation, and generalization of detailed neuronal models. *Patterns (N Y)* 4: 100855, 2023. doi:10.1016/j.patter.2023.100855.

25. **Roy A**, **Narayanan R.** Spatial information transfer in hippocampal place cells depends on trial-to-trial variability, symmetry of place-field firing, and biophysical heterogeneities. *Neural Netw* 142: 636–660, 2021. doi:10.1016/j.neunet.2021.07.026.

26. **Basak R**, **Narayanan R.** Spatially dispersed synapses yield sharply-tuned place cell responses through dendritic spike initiation. *J Physiol* 596: 4173–4205, 2018. doi:10.1113/JP275310.

27. **Basak R**, **Narayanan R.** Robust emergence of sharply tuned place-cell responses in hippocampal neurons with structural and biophysical heterogeneities. *Brain Struct Funct* 225: 567–590, 2020. doi:10.1007/s00429-019-02018-0.

28. **Edelman GM**, **Gally JA.** Degeneracy and complexity in biological systems. *Proc Natl Acad Sci USA* 98: 13763–13768, 2001. doi:10.1073/pnas.231499798.

29. **Mainen ZF**, **Sejnowski TJ.** Influence of dendritic structure on firing pattern in model neocortical neurons. *Nature* 382: 363–366, 1996. doi:10.1038/382363a0.

30. **Krichmar JL**, **Nasuto SJ**, **Scorcioni R**, **Washington SD**, **Ascoli GA.** Effects of dendritic morphology on CA3 pyramidal cell electrophysiology: a simulation study. *Brain Res* 941: 11–28, 2002. doi:10.1016/s0006-8993(02)02488-5.

31. **Narayanan R**, **Chattarji S.** Computational analysis of the impact of chronic stress on intrinsic and synaptic excitability in the hippocampus. *J Neurophysiol* 103: 3070–3083, 2010. doi:10.1152/jn.00913.2009.

32. **Dhupia N**, **Rathour RK**, **Narayanan R.** Dendritic atrophy constricts functional maps in resonance and impedance properties of hippocampal model neurons. *Front Cell Neurosci* 8: 456, 2014. doi:10.3389/fncel.2014.00456.

33. **Yang J**, **Shakil H**, **Ratté S**, **Prescott SA.** Minimal requirements for a neuron to coregulate many properties and the implications for ion channel correlations and robustness. *eLife* 11: e72875, 2022. doi:10.7554/eLife.72875.

34. **Hervieu GJ**, **Cluderay JE**, **Gray CW**, **Green PJ**, **Ranson JL**, **Randall AD**, **Meadows HJ.** Distribution and expression of TREK-1, a two-pore-domain potassium channel, in the adult rat CNS. *Neuroscience* 103: 899–919, 2001. doi:10.1016/s0306-4522(01)00030-6.

35. **Gabriel A**, **Abdallah M**, **Yost CS**, **Winegar BD**, **Kindler CH.** Localization of the tandem pore domain K+ channel KCNK5 (TASK-2) in the rat central nervous system. *Brain Res Mol Brain Res* 98: 153–163, 2002. doi:10.1016/s0169-328x(01)00330-8.

36. **Yarishkin O**, **Lee DY**, **Kim E**, **Cho CH**, **Choi JH**, **Lee CJ**, **Hwang EM**, **Park JY.** TWIK-1 contributes to the intrinsic excitability of dentate granule cells in mouse hippocampus. *Mol Brain* 7: 80, 2014. doi:10.1186/s13041-014-0080-z.

37. **Ishihara K**, **Yan DH.** Low-affinity spermine block mediating outward currents through Kir2.1 and Kir2.2 inward rectifier potassium channels. *J Physiol* 583: 891–908, 2007. doi:10.1113/jphysiol.2007.136028.

38. **Panama BK**, **Lopatin AN.** Differential polyamine sensitivity in inwardly rectifying Kir2 potassium channels. *J Physiol* 571: 287–302, 2006. doi:10.1113/jphysiol.2005.097741.

39. **Yan DH**, **Ishihara K.** Two Kir2.1 channel populations with different sensitivities to Mg(2+) and polyamine block: a model for the cardiac strong inward rectifier K(+) channel. *J Physiol* 563: 725–744, 2005. doi:10.1113/jphysiol.2004.079186.

40. **Lopatin AN**, **Makhina EN**, **Nichols CG.** The mechanism of inward rectification of potassium channels: "long-pore plugging" by cytoplasmic polyamines. *J Gen Physiol* 106: 923–955, 1995. doi:10.1085/jgp.106.5.923.

41. **Schmidt-Hieber C**, **Bischofberger J.** Fast sodium channel gating supports localized and efficient axonal action potential initiation. *J Neurosci* 30: 10233–10242, 2010. doi:10.1523/JNEUROSCI.6335-09.2010.

42. **Kress GJ**, **Dowling MJ**, **Eisenman LN**, **Mennerick S.** Axonal sodium channel distribution shapes the depolarized action potential threshold of dentate granule neurons. *Hippocampus* 20: 558–571, 2010. doi:10.1002/hipo.20667.

43. **Christie MJ**, **Adelman JP**, **Douglass J**, **North RA.** Expression of a cloned rat brain potassium channel in Xenopus oocytes. *Science* 244: 221–224, 1989. doi:10.1126/science.2539643.

44. **Wissmann R**, **Bildl W**, **Oliver D**, **Beyermann M**, **Kalbitzer HR**, **Bentrop D**, **Fakler B.** Solution structure and function of the "tandem inactivation domain" of the neuronal A-type potassium channel Kv1.4. *J Biol Chem* 278: 16142–16150, 2003. doi:10.1074/jbc.M210191200.

45. **Barghaan J**, **Tozakidou M**, **Ehmke H**, **Bähring R.** Role of N-terminal domain and accessory subunits in controlling deactivation-inactivation coupling of Kv4.2 channels. *Biophys J* 94: 1276–1294, 2008. doi:10.1529/biophysj.107.111344.

46. **Rudy B**, **Sen K**, **Vega-Saenz de Miera E**, **Lau D**, **Ried T**, **Ward DC.** Cloning of a human cDNA expressing a high voltage-activating, TEA-sensitive, type-A K+ channel which maps to chromosome 1 band p21. *J Neurosci Res* 29: 401–412, 1991. doi:10.1002/jnr.490290316.

47. **Schröter KH**, **Ruppersberg JP**, **Wunder F**, **Rettig J**, **Stocker M**, **Pongs O.** Cloning and functional expression of a TEA-sensitive A-type potassium channel from rat brain. *FEBS Lett* 278: 211–216, 1991. doi:10.1016/0014-5793(91)80119-n.

48. **Rettig J**, **Wunder F**, **Stocker M**, **Lichtinghagen R**, **Mastiaux F**, **Beckh S**, **Kues W**, **Pedarzani P**, **Schröter KH**, **Ruppersberg JP.** Characterization of a Shaw-related potassium channel family in rat brain. *EMBO J* 11: 2473–2486, 1992. doi:10.1002/j.1460-2075.1992.tb05312.x.

49. **Vega-Saenz de Miera E**, **Moreno H**, **Fruhling D**, **Kentros C**, **Rudy B.** Cloning of ShIII (Shaw-like) cDNAs encoding a novel high-voltage-activating, TEA-sensitive, type-A K$^+$ channel. *Proc Biol Sci* 248: 9–18, 1992. doi:10.1098/rspb.1992.0036.

50. **Riazanski V**, **Becker A**, **Chen J**, **Sochivko D**, **Lie A**, **Wiestler OD**, **Elger CE**, **Beck H.** Functional and molecular analysis of transient voltage-dependent K+ currents in rat hippocampal granule cells. *J Physiol* 537: 391–406, 2001. doi:10.1111/j.1469-7793.2001.00391.x.

51. **Mateos-Aparicio P**, **Murphy R**, **Storm JF.** Complementary functions of SK and Kv7/M potassium channels in excitability control and synaptic integration in rat hippocampal dentate granule cells. *J Physiol* 592: 669–693, 2014. doi:10.1113/jphysiol.2013.267872.

52. **Stegen M**, **Kirchheim F**, **Hanuschkin A**, **Staszewski O**, **Veh RW**, **Wolfart J.** Adaptive intrinsic plasticity in human dentate gyrus granule cells during temporal lobe epilepsy. *Cereb Cortex* 22: 2087–2101, 2012. doi:10.1093/cercor/bhr294.

53. **Fox AP**, **Nowycky MC**, **Tsien RW.** Kinetic and pharmacological properties distinguishing three types of calcium currents in chick sensory neurones. *J Physiol* 394: 149–172, 1987. doi:10.1113/jphysiol.1987.sp016864.

54. **Burgess DE**, **Crawford O**, **Delisle BP**, **Satin J.** Mechanism of inactivation gating of human T-type (low-voltage activated) calcium channels. *Biophys J* 82: 1894–1906, 2002. doi:10.1016/S0006-3495(02)75539-2.

55. **Evans RC**, **Maniar YM**, **Blackwell KT.** Dynamic modulation of spike timing-dependent calcium influx during corticostriatal upstates. *J Neurophysiol* 110: 1631–1645, 2013. doi:10.1152/jn.00232.2013.

56. **Jaffe DB**, **Wang B**, **Brenner R.** Shaping of action potentials by type I and type II large-conductance Ca(2)+-activated K$^+$ channels. *Neuroscience* 192: 205–218, 2011. doi:10.1016/j.neuroscience.2011.06.028.

57. **Solinas S**, **Forti L**, **Cesana E**, **Mapelli J**, **De Schutter E**, **D'Angelo E.** Computational reconstruction of pacemaking and intrinsic electroresponsiveness in cerebellar Golgi cells. *Front Cell Neurosci* 1: 2, 2007. doi:10.3389/neuro.03.002.2007.

58. **Hirschberg B**, **Maylie J**, **Adelman JP**, **Marrion NV.** Gating properties of single SK channels in hippocampal CA1 pyramidal neurons. *Biophys J* 77: 1905–1913, 1999. doi:10.1016/S0006-3495(99)77032-3.

59. **Hodgkin AL**, **Huxley AF.** A quantitative description of membrane current and its application to conduction and excitation in nerve. *J Physiol* 117: 500–544, 1952. doi:10.1113/jphysiol.1952.sp004764.

60. **Anwar H**, **Roome CJ**, **Nedelescu H**, **Chen W**, **Kuhn B**, **De Schutter E.** Dendritic diameters affect the spatial variability of intracellular calcium dynamics in computer models. *Front Cell Neurosci* 8: 168, 2014. doi:10.3389/fncel.2014.00168.

61. **Jackson MB**, **Redman SJ.** Calcium dynamics, buffering, and buffer saturation in the boutons of dentate granule-cell axons in the hilus. *J Neurosci* 23: 1612–1621, 2003. doi:10.1523/JNEUROSCI.23-05-01612.2003.

62. **Stocca G**, **Schmidt-Hieber C**, **Bischofberger J.** Differential dendritic Ca2+ signalling in young and mature hippocampal granule cells. *J Physiol* 586: 3795–3811, 2008. doi:10.1113/jphysiol.2008.155739.

63. **Krueppel R**, **Remy S**, **Beck H.** Dendritic integration in hippocampal dentate granule cells. *Neuron* 71: 512–528, 2011. doi:10.1016/j.neuron.2011.05.043.

64. **Carnevale NT**, **Hines ML.** *The NEURON Book.* Cambridge, UK: Cambridge University Press, 2006.

65. **Narayanan R**, **Johnston D.** Long-term potentiation in rat hippocampal neurons is accompanied by spatially widespread changes in intrinsic oscillatory dynamics and excitability. *Neuron* 56: 1061–1075, 2007. doi:10.1016/j.neuron.2007.10.033.

66. **Narayanan R**, **Johnston D.** The h channel mediates location dependence and plasticity of intrinsic phase response in rat hippocampal neurons. *J Neurosci* 28: 5846–5860, 2008. doi:10.1523/JNEUROSCI.0835-08.2008.

67. **Basak R**, **Narayanan R.** Active dendrites regulate the spatiotemporal spread of signaling microdomains. *PLoS Comput Biol* 14: e1006485, 2018. doi:10.1371/journal.pcbi.1006485.

68. **Jain A**, **Narayanan R.** Degeneracy in the emergence of spike-triggered average of hippocampal pyramidal neurons. *Sci Rep* 10: 374, 2020. doi:10.1038/s41598-019-57243-8.

69. **Sinha M**, **Narayanan R.** Active dendrites and local field potentials: biophysical mechanisms and computational explorations. *Neuroscience* 489: 111–142, 2022. doi:10.1016/j.neuroscience.2021.08.035.

70. **Anirudhan A**, **Narayanan R.** Analogous synaptic plasticity profiles emerge from disparate channel combinations. *J Neurosci* 35: 4691–4705, 2015. doi:10.1523/JNEUROSCI.4223-14.2015.

71. **Shridhar S**, **Mishra P**, **Narayanan R.** Dominant role of adult neurogenesis-induced structural heterogeneities in driving plasticity heterogeneity in dentate gyrus granule cells. *Hippocampus* 32: 488–516, 2022. doi:10.1002/hipo.23422.

72. **Mukunda CL**, **Narayanan R.** Degeneracy in the regulation of short-term plasticity and synaptic filtering by presynaptic mechanisms. *J Physiol* 595: 2611–2637, 2017. doi:10.1113/JP273482.

73. **Srikanth S**, **Narayanan R.** Variability in state-dependent plasticity of intrinsic properties during cell-autonomous self-regulation of calcium homeostasis in hippocampal model neurons. *eNeuro* 2: ENEURO.0053-0015.2015, 2015. doi:10.1523/ENEURO.0053-15.2015.

74. **Srikanth S**, **Narayanan R.** Heterogeneous off-target impact of ion-channel deletion on intrinsic properties of hippocampal model neurons that self-regulate calcium. *Front Cell Neurosci* 17: 1241450, 2023. doi:10.3389/fncel.2023.1241450.

75. **Seenivasan P**, **Narayanan R.** Efficient phase coding in hippocampal place cells. *Phys Rev Res* 2: 033393, 2020. doi:10.1103/PhysRevResearch.2.033393.

76. **Van der Maaten L**, **Hinton G.** Visualizing data using t-SNE. *J Mach Learn Res* 9: 2579−2605, 2008. https://jmlr.org/papers/v9/vandermaaten08a.html.

77. **McInnes L**, **Healy J**, **Melville J.** UMAP: Uniform manifold approximation and projection for dimension reduction (Preprint). arXiv: 80203426, 2018. doi:10.48550/arXiv.1802.03426.

78. **Moon KR**, **van Dijk D**, **Wang Z**, **Gigante S**, **Burkhardt DB**, **Chen WS**, **Yim K**, **Elzen AVD**, **Hirn MJ**, **Coifman RR**, **Ivanova NB**, **Wolf G**, **Krishnaswamy S.** Visualizing structure and transitions in high-dimensional biological data. *Nat Biotechnol* 37: 1482–1492, 2019 [Erratum in Nat Biotechnol 38: 108, 2020]. doi:10.1038/s41587-019-0336-3.

79. **Lloyd S.** Least squares quantization in PCM. *IEEE Trans Inform Theory* 28: 129–137, 1982. doi:10.1109/TIT.1982.1056489.

80. **Mahalanobis PC.** On the generalised distance in statistics. *Proc Natl Inst Sci India* 2: 49–55, 1936. https://www.jstor.org/stable/48723335.

81. **Ye GL**, **Yi S**, **Gamkrelidze G**, **Pasternak JF**, **Trommer BL.** AMPA and NMDA receptor-mediated currents in developing dentate gyrus granule cells. *Brain Res Dev Brain Res* 155: 26–32, 2005. doi:10.1016/j.devbrainres.2004.12.002.

82. **Goldman DE.** Potential, impedance, and rectification in membranes. *J Gen Physiol* 27: 37–60, 1943. doi:10.1085/jgp.27.1.37.

83. **Hodgkin AL**, **Katz B.** The effect of sodium ions on the electrical activity of giant axon of the squid. *J Physiol* 108: 37–77, 1949. doi:10.1113/jphysiol.1949.sp004310.

84. **Narayanan R**, **Johnston D.** The h current is a candidate mechanism for regulating the sliding modification threshold in a BCM-like synaptic learning rule. *J Neurophysiol* 104: 1020–1033, 2010. doi:10.1152/jn.01129.2009.

85. **Evans JD.** *Straightforward Statistics for the Behavioral Sciences.* Boston, MA: Brooks/Cole Pub Co, 1996.

86. **Yang J**, **Prescott SA.** Homeostatic regulation of neuronal function: importance of degeneracy and pleiotropy. *Front Cell Neurosci* 17: 1184563, 2023. doi:10.3389/fncel.2023.1184563.

87. **Mittal D**, **Narayanan R.** Network motifs in cellular neurophysiology. *Trends Neurosci* 47: 506–521, 2024. doi:10.1016/j.tins.2024.04.008.

88. **Tononi G**, **Sporns O**, **Edelman GM.** A measure for brain complexity: relating functional segregation and integration in the nervous system. *Proc Natl Acad Sci USA* 91: 5033–5037, 1994. doi:10.1073/pnas.91.11.5033.

89. **Sporns O**, **Tononi G**, **Edelman GM.** Connectivity and complexity: the relationship between neuroanatomy and brain dynamics. *Neural Netw* 13: 909–922, 2000. doi:10.1016/s0893-6080(00)00053-8.

90. **Marom S**, **Marder E.** A biophysical perspective on the resilience of neuronal excitability across timescales. *Nat Rev Neurosci* 24: 640–652, 2023. doi:10.1038/s41583-023-00730-9.

91. **Gjorgjieva J**, **Drion G**, **Marder E.** Computational implications of biophysical diversity and multiple timescales in neurons and synapses for circuit performance. *Curr Opin Neurobiol* 37: 44–52, 2016. doi:10.1016/j.conb.2015.12.008.

92. **Mishra P**, **Narayanan R.** Stable continual learning through structured multiscale plasticity manifolds. *Curr Opin Neurobiol* 70: 51–63, 2021. doi:10.1016/j.conb.2021.07.009.

93. **Price CJ**, **Friston KJ.** Degeneracy and cognitive anatomy. *Trends Cogn Sci* 6: 416–421, 2002. doi:10.1016/s1364-6613(02)01976-9.

94. **Leonardo A.** Degenerate coding in neural systems. *J Comp Physiol A Neuroethol Sens Neural Behav Physiol* 191: 995–1010, 2005. doi:10.1007/s00359-005-0026-0.

95. **Prinz AA**, **Bucher D**, **Marder E.** Similar network activity from disparate circuit parameters. *Nat Neurosci* 7: 1345–1352, 2004. doi:10.1038/nn1352.

96. **Seenivasan P**, **Narayanan R.** Efficient information coding and degeneracy in the nervous system. *Curr Opin Neurobiol* 76: 102620, 2022. doi:10.1016/j.conb.2022.102620.

97. **Rathour RK**, **Malik R**, **Narayanan R.** Transient potassium channels augment degeneracy in hippocampal active dendritic spectral tuning. *Sci Rep* 6: 24678, 2016. doi:10.1038/srep24678.

98. **Ashhad S**, **Narayanan R.** Quantitative interactions between the A-type K+ current and inositol trisphosphate receptors regulate intraneuronal Ca2+ waves and synaptic plasticity. *J Physiol* 591: 1645–1669, 2013. doi:10.1113/jphysiol.2012.245688.

99. **Pastoll H**, **Garden DL**, **Papastathopoulos I**, **Sürmeli G**, **Nolan MF.** Inter- and intra-animal variation in the integrative properties of stellate cells in the medial entorhinal cortex. *eLife* 9: e52258, 2020. doi:10.7554/eLife.52258.

100. **Cropper EC**, **Dacks AM**, **Weiss KR.** Consequences of degeneracy in network function. *Curr Opin Neurobiol* 41: 62–67, 2016. doi:10.1016/j.conb.2016.07.008.

101. **Kamaleddin MA.** Degeneracy in the nervous system: from neuronal excitability to neural coding. *Bioessays* 44: e2100148, 2022. doi:10.1002/bies.202100148.

102. **Mason PH.** Degeneracy at multiple levels of complexity. *Biol Theory* 5: 277–288, 2010. doi:10.1162/BIOT_a_00041.

103. **Mason PH**, **Domínguez DJ**, **Winter B**, **Grignolio A.** Hidden in plain view: degeneracy in complex systems. *Biosystems* 128: 1–8, 2015. doi:10.1016/j.biosystems.2014.12.003.

104. **Stöber TM**, **Batulin D**, **Triesch J**, **Narayanan R**, **Jedlicka P.** Degeneracy in epilepsy: multiple routes to hyperexcitable brain circuits and their repair. *Commun Biol* 6: 479, 2023. doi:10.1038/s42003-023-04823-0.

105. **Whitacre J**, **Bender A.** Degeneracy: a design principle for achieving robustness and evolvability. *J Theor Biol* 263: 143–153, 2010. doi:10.1016/j.jtbi.2009.11.008.

106. **Whitacre JM.** Degeneracy: a link between evolvability, robustness and complexity in biological systems. *Theor Biol Med Model* 7: 6, 2010. doi:10.1186/1742-4682-7-6.

107. **Marder E**, **Goaillard JM.** Variability, compensation and homeostasis in neuron and network function. *Nat Rev Neurosci* 7: 563–574, 2006. doi:10.1038/nrn1949.

108. **O'Leary T.** Homeostasis, failure of homeostasis and degenerate ion channel regulation. *Curr Opin Physiol* 2: 129–138, 2018. doi:10.1016/j.cophys.2018.01.006.

109. **Magee JC.** Dendritic hyperpolarization-activated currents modify the integrative properties of hippocampal CA1 pyramidal neurons. *J Neurosci* 18: 7613–7624, 1998. doi:10.1523/JNEUROSCI.18-19-07613.1998.

110. **Magee JC.** Dendritic integration of excitatory synaptic input. *Nat Rev Neurosci* 1: 181–190, 2000. doi:10.1038/35044552.

111. **Magee JC**, **Cook EP.** Somatic EPSP amplitude is independent of synapse location in hippocampal pyramidal neurons. *Nat Neurosci* 3: 895–903, 2000. doi:10.1038/78800.

112. **Magee JC**, **Johnston D.** Synaptic activation of voltage-gated channels in the dendrites of hippocampal pyramidal neurons. *Science* 268: 301–304, 1995. doi:10.1126/science.7716525.

113. **Hoffman DA**, **Magee JC**, **Colbert CM**, **Johnston D.** K+ channel regulation of signal propagation in dendrites of hippocampal pyramidal neurons. *Nature* 387: 869–875, 1997. doi:10.1038/43119.

114. **Vaidya SP**, **Johnston D.** Temporal synchrony and gamma-to-theta power conversion in the dendrites of CA1 pyramidal neurons. *Nat Neurosci* 16: 1812–1820, 2013. doi:10.1038/nn.3562.

115. **Hu H**, **Vervaeke K**, **Graham LJ**, **Storm JF.** Complementary theta resonance filtering by two spatially segregated mechanisms in CA1 hippocampal pyramidal neurons. *J Neurosci* 29: 14472–14483, 2009. doi:10.1523/JNEUROSCI.0187-09.2009.

116. **Hu H**, **Vervaeke K**, **Storm JF.** M-channels (Kv7/KCNQ channels) that regulate synaptic integration, excitability, and spike pattern of CA1 pyramidal cells are located in the perisomatic region. *J Neurosci* 27: 1853–1867, 2007. doi:10.1523/JNEUROSCI.4463-06.2007.

117. **Rathour RK**, **Narayanan R.** Influence fields: a quantitative framework for representation and analysis of active dendrites. *J Neurophysiol* 107: 2313–2334, 2012. doi:10.1152/jn.00846.2011.

118. **Golding NL**, **Mickus TJ**, **Katz Y**, **Kath WL**, **Spruston N.** Factors mediating powerful voltage attenuation along CA1 pyramidal neuron dendrites. *J Physiol* 568: 69–82, 2005. doi:10.1113/jphysiol.2005.086793.

119. **Otopalik AG**, **Goeritz ML**, **Sutton AC**, **Brookings T**, **Guerini C**, **Marder E.** Sloppy morphological tuning in identified neurons of the crustacean stomatogastric ganglion. *eLife* 6: e22352, 2017. doi:10.7554/eLife.22352.

120. **Otopalik AG**, **Pipkin J**, **Marder E.** Neuronal morphologies built for reliable physiology in a rhythmic motor circuit. *eLife* 8: e41728, 2019. doi:10.7554/eLife.41728.

121. **Franci A**, **O'Leary T**, **Golowasch J.** Positive dynamical networks in neuronal regulation: how tunable variability coexists with robustness. *IEEE Control Syst Lett* 4: 946–951, 2020. doi:10.1109/LCSYS.2020.2997214.

122. **O'Leary T**, **Marder E.** Temperature-robust neural function from activity-dependent ion channel regulation. *Curr Biol* 26: 2935–2941, 2016. doi:10.1016/j.cub.2016.08.061.

123. **O'Leary T**, **Williams AH**, **Franci A**, **Marder E.** Cell types, network homeostasis, and pathological compensation from a biologically plausible ion channel expression model. *Neuron* 82: 809–821, 2014 [Erratum in Neuron 88: 1308, 2015]. doi:10.1016/j.neuron.2014.04.002.

124. **Ratliff J**, **Franci A**, **Marder E**, **O'Leary T.** Neuronal oscillator robustness to multiple global perturbations. *Biophys J* 120: 1454–1468, 2021. doi:10.1016/j.bpj.2021.01.038.

125. **Jedlicka P**, **Bird AD**, **Cuntz H.** Pareto optimality, economy-effectiveness trade-offs and ion channel degeneracy: improving population modelling for single neurons. *Open Biol* 12: 220073, 2022. doi:10.1098/rsob.220073.

126. **Strange BA**, **Witter MP**, **Lein ES**, **Moser EI.** Functional organization of the hippocampal longitudinal axis. *Nat Rev Neurosci* 15: 655–669, 2014. doi:10.1038/nrn3785.

127. **van Groen T**, **Miettinen P**, **Kadish I.** The entorhinal cortex of the mouse: organization of the projection to the hippocampal formation. *Hippocampus* 13: 133–149, 2003. doi:10.1002/hipo.10037.

128. **Schmidt B**, **Marrone DF**, **Markus EJ.** Disambiguating the similar: the dentate gyrus and pattern separation. *Behav Brain Res* 226: 56–65, 2012. doi:10.1016/j.bbr.2011.08.039.

129. **Desmond NL**, **Levy WB.** Granule cell dendritic spine density in the rat hippocampus varies with spine shape and location. *Neurosci Lett* 54: 219–224, 1985. doi:10.1016/s0304-3940(85)80082-3.

130. **Desmond NL**, **Levy WB.** A quantitative anatomical study of the granule cell dendritic fields of the rat dentate gyrus using a novel probabilistic method. *J Comp Neurol* 212: 131–145, 1982. doi:10.1002/cne.902120204.

131. **Lee AR**, **Kim JH**, **Cho E**, **Kim M**, **Park M.** Dorsal and ventral hippocampus differentiate in functional pathways and differentially associate with neurological disease-related genes during postnatal development. *Front Mol Neurosci* 10: 331, 2017. doi:10.3389/fnmol.2017.00331.

132. **Cembrowski MS**, **Spruston N.** Heterogeneity within classical cell types is the rule: lessons from hippocampal pyramidal neurons. *Nat Rev Neurosci* 20: 193–204, 2019. doi:10.1038/s41583-019-0125-5.

133. **Botterill JJ**, **Gerencer KJ**, **Vinod KY**, **Alcantara-Gonzalez D**, **Scharfman HE.** Dorsal and ventral mossy cells differ in their axonal projections throughout the dentate gyrus of the mouse hippocampus. *Hippocampus* 31: 522–539, 2021. doi:10.1002/hipo.23314.

134. **Schreurs A**, **Sabanov V**, **Balschun D.** Distinct properties of long-term potentiation in the dentate gyrus along the dorsoventral axis: influence of age and inhibition. *Sci Rep* 7: 5157, 2017. doi:10.1038/s41598-017-05358-1.

135. **Surges R**, **Kukley M**, **Brewster A**, **Rüschenschmidt C**, **Schramm J**, **Baram TZ**, **Beck H**, **Dietrich D.** Hyperpolarization-activated cation

current Ih of dentate gyrus granule cells is upregulated in human and rat temporal lobe epilepsy. *Biochem Biophys Res Commun* 420: 156–160, 2012. doi:10.1016/j.bbrc.2012.02.133.

136. **Bender RA, Soleymani SV, Brewster AL, Nguyen ST, Beck H, Mathern GW, Baram TZ.** Enhanced expression of a specific hyperpolarization-activated cyclic nucleotide-gated cation channel (HCN) in surviving dentate gyrus granule cells of human and experimental epileptic hippocampus. *J Neurosci* 23: 6826–6836, 2003. doi:10.1523/JNEUROSCI.23-17-06826.2003.

137. **Young CC, Stegen M, Bernard R, Müller M, Bischofberger J, Veh RW, Haas CA, Wolfart J.** Upregulation of inward rectifier K + (Kir2) channels in dentate gyrus granule cells in temporal lobe epilepsy. *J Physiol* 587: 4213–4233, 2009. doi:10.1113/jphysiol.2009.170746.

138. **Stegen M, Young CC, Haas CA, Zentner J, Wolfart J.** Increased leak conductance in dentate gyrus granule cells of temporal lobe epilepsy patients with Ammon's horn sclerosis. *Epilepsia* 50: 646–653, 2009. doi:10.1111/j.1528-1167.2009.02025.x.

139. **Artinian J, Peret A, Marti G, Epsztein J, Crépel V.** Synaptic kainate receptors in interplay with INaP shift the sparse firing of dentate granule cells to a sustained rhythmic mode in temporal lobe epilepsy. *J Neurosci* 31: 10811–10818, 2011. doi:10.1523/JNEUROSCI.0388-11.2011.

140. **Ellerkmann RK, Remy S, Chen J, Sochivko D, Elger CE, Urban BW, Becker A, Beck H.** Molecular and functional changes in voltage-dependent Na(+) channels following pilocarpine-induced status epilepticus in rat dentate granule cells. *Neuroscience* 119: 323–333, 2003. doi:10.1016/s0306-4522(03)00168-4.

141. **Epsztein J, Sola E, Represa A, Ben-Ari Y, Crépel V.** A selective interplay between aberrant EPSPKA and INaP reduces spike timing precision in dentate granule cells of epileptic rats. *Cereb Cortex* 20: 898–911, 2010. doi:10.1093/cercor/bhp156.

142. **Wossink J, Karst H, Mayboroda O, Joëls M.** Morphological and functional properties of rat dentate granule cells after adrenalectomy. *Neuroscience* 108: 263–272, 2001. doi:10.1016/s0306-4522(01)00414-6.

143. **Verina T, Rohde CA, Guilarte TR.** Environmental lead exposure during early life alters granule cell neurogenesis and morphology in the hippocampus of young adult rats. *Neuroscience* 145: 1037–1047, 2007. doi:10.1016/j.neuroscience.2006.12.040.

144. **Perederiy JV, Westbrook GL.** Structural plasticity in the dentate gyrus- revisiting a classic injury model. *Front Neural Circuits* 7: 17, 2013. doi:10.3389/fncir.2013.00017.

145. **Zhao C, Deng W, Gage FH.** Mechanisms and functional implications of adult neurogenesis. *Cell* 132: 645–660, 2008. doi:10.1016/j.cell.2008.01.033.

146. **Aimone JB, Li Y, Lee SW, Clemenson GD, Deng W, Gage FH.** Regulation and function of adult neurogenesis: from genes to cognition. *Physiol Rev* 94: 991–1026, 2014. doi:10.1152/physrev.00004.2014.

147. **Doetsch F, Hen R.** Young and excitable: the function of new neurons in the adult mammalian brain. *Curr Opin Neurobiol* 15: 121–128, 2005. doi:10.1016/j.conb.2005.01.018.

148. **Altman J, Das GD.** Autoradiographic and histological evidence of postnatal hippocampal neurogenesis in rats. *J Comp Neurol* 124: 319–335, 1965. doi:10.1002/cne.901240303.

149. **Beining M, Jungenitz T, Radic T, Deller T, Cuntz H, Jedlicka P, Schwarzacher SW.** Adult-born dentate granule cells show a critical period of dendritic reorganization and are distinct from developmentally born cells. *Brain Struct Funct* 222: 1427–1446, 2017. doi:10.1007/s00429-016-1285-y.

150. **Cole JD, Espinueva DF, Seib DR, Ash AM, Cooke MB, Cahill SP, O'Leary TP, Kwan SS, Snyder JS.** Adult-born hippocampal neurons undergo extended development and are morphologically distinct from neonatally-born neurons. *J Neurosci* 40: 5740–5756, 2020. doi:10.1523/JNEUROSCI.1665-19.2020.

151. **Dieni CV, Nietz AK, Panichi R, Wadiche JI, Overstreet-Wadiche L.** Distinct determinants of sparse activation during granule cell maturation. *J Neurosci* 33: 19131–19142, 2013. doi:10.1523/JNEUROSCI.2289-13.2013.

152. **Dieni CV, Panichi R, Aimone JB, Kuo CT, Wadiche JI, Overstreet-Wadiche L.** Low excitatory innervation balances high intrinsic excitability of immature dentate neurons. *Nat Commun* 7: 11313, 2016. doi:10.1038/ncomms11313.

153. **Li L, Sultan S, Heigele S, Schmidt-Salzmann C, Toni N, Bischofberger J.** Silent synapses generate sparse and orthogonal action potential firing in adult-born hippocampal granule cells. *eLife* 6: e23612, 2017. doi:10.7554/eLife.23612.

154. **Lodge M, Bischofberger J.** Synaptic properties of newly generated granule cells support sparse coding in the adult hippocampus. *Behav Brain Res* 372: 112036, 2019. doi:10.1016/j.bbr.2019.112036.

155. **Mittag M, Mediavilla L, Remy S, Cuntz H, Jedlicka P.** Modelling the contributions to hyperexcitability in a mouse model of Alzheimer's disease. *J Physiol* 601: 3403–3437, 2023. doi:10.1113/JP283401.

156. **Ratté S, Prescott SA.** Afferent hyperexcitability in neuropathic pain and the inconvenient truth about its degeneracy. *Curr Opin Neurobiol* 36: 31–37, 2016. doi:10.1016/j.conb.2015.08.007.

157. **Ratté S, Zhu Y, Lee KY, Prescott SA.** Criticality and degeneracy in injury-induced changes in primary afferent excitability and the implications for neuropathic pain. *eLife* 3: e02370, 2014. doi:10.7554/eLife.02370.

158. **Cayco-Gajic NA, Clopath C, Silver RA.** Sparse synaptic connectivity is required for decorrelation and pattern separation in feedforward networks. *Nat Commun* 8: 1116, 2017. doi:10.1038/s41467-017-01109-y.

159. **Moreno-Bote R, Beck J, Kanitscheider I, Pitkow X, Latham P, Pouget A.** Information-limiting correlations. *Nat Neurosci* 17: 1410–1417, 2014. doi:10.1038/nn.3807.

160. **Wick SD, Wiechert MT, Friedrich RW, Riecke H.** Pattern orthogonalization via channel decorrelation by adaptive networks. *J Comput Neurosci* 28: 29–45, 2010. doi:10.1007/s10827-009-0183-1.

161. **Bakker A, Kirwan CB, Miller M, Stark CE.** Pattern separation in the human hippocampal CA3 and dentate gyrus. *Science* 319: 1640–1642, 2008. doi:10.1126/science.1152882.

162. **Clelland CD, Choi M, Romberg C, Clemenson GD Jr, Fragniere A, Tyers P, Jessberger S, Saksida LM, Barker RA, Gage FH, Bussey TJ.** A functional role for adult hippocampal neurogenesis in spatial pattern separation. *Science* 325: 210–213, 2009. doi:10.1126/science.1173215.

163. **Deng W, Aimone JB, Gage FH.** New neurons and new memories: how does adult hippocampal neurogenesis affect learning and memory? *Nat Rev Neurosci* 11: 339–350, 2010. doi:10.1038/nrn2822.

164. **Leutgeb JK, Leutgeb S, Moser MB, Moser EI.** Pattern separation in the dentate gyrus and CA3 of the hippocampus. *Science* 315: 961–966, 2007. doi:10.1126/science.1135801.

165. **McHugh TJ, Jones MW, Quinn JJ, Balthasar N, Coppari R, Elmquist JK, Lowell BB, Fanselow MS, Wilson MA, Tonegawa S.** Dentate gyrus NMDA receptors mediate rapid pattern separation in the hippocampal network. *Science* 317: 94–99, 2007. doi:10.1126/science.1140263.

166. **Sahay A, Wilson DA, Hen R.** Pattern separation: a common function for new neurons in hippocampus and olfactory bulb. *Neuron* 70: 582–588, 2011. doi:10.1016/j.neuron.2011.05.012.

167. **Vivar C, Potter MC, Choi J, Lee JY, Stringer TP, Callaway EM, Gage FH, Suh H, van Praag H.** Monosynaptic inputs to new neurons in the dentate gyrus. *Nat Commun* 3: 1107, 2012. doi:10.1038/ncomms2101.

168. **Wu MV, Sahay A, Duman RS, Hen R.** Functional differentiation of adult-born neurons along the septotemporal axis of the dentate gyrus. *Cold Spring Harb Perspect Biol* 7: a018978, 2015. doi:10.1101/cshperspect.a018978.

169. **Chavlis S, Petrantonakis PC, Poirazi P.** Dendrites of dentate gyrus granule cells contribute to pattern separation by controlling sparsity. *Hippocampus* 27: 89–110, 2017 [Erratum in Hippocampus 27: 477–478, 2017]. doi:10.1002/hipo.22675.

170. **Mishra P, Narayanan R.** Conjunctive changes in multiple ion channels mediate activity-dependent intrinsic plasticity in hippocampal granule cells. *iScience* 25: 103922, 2022. doi:10.1016/j.isci.2022.103922.

171. **Liu X, Ramirez S, Pang PT, Puryear CB, Govindarajan A, Deisseroth K, Tonegawa S.** Optogenetic stimulation of a hippocampal engram activates fear memory recall. *Nature* 484: 381–385, 2012. doi:10.1038/nature11028.

172. **Park S, Kramer EE, Mercaldo V, Rashid AJ, Insel N, Frankland PW, Josselyn SA.** Neuronal allocation to a hippocampal engram. *Neuropsychopharmacology* 41: 2987–2993, 2016. doi:10.1038/npp.2016.73.

173. **Ramirez S, Liu X, Lin PA, Suh J, Pignatelli M, Redondo RL, Ryan TJ, Tonegawa S.** Creating a false memory in the hippocampus. *Science* 341: 387–391, 2013. doi:10.1126/science.1239073.

174. **Ramirez S, Liu X, MacDonald CJ, Moffa A, Zhou J, Redondo RL, Tonegawa S.** Activating positive memory engrams suppresses

depression-like behaviour. *Nature* 522: 335–339, 2015. doi:10.1038/nature14514.

175. **Redondo RL**, **Kim J**, **Arons AL**, **Ramirez S**, **Liu X**, **Tonegawa S.** Bidirectional switch of the valence associated with a hippocampal contextual memory engram. *Nature* 513: 426–430, 2014. doi:10.1038/nature13725.

176. **Roy DS**, **Arons A**, **Mitchell TI**, **Pignatelli M**, **Ryan TJ**, **Tonegawa S.** Memory retrieval by activating engram cells in mouse models of early Alzheimer's disease. *Nature* 531: 508–512, 2016. doi:10.1038/nature17172.

177. **Titley HK**, **Brunel N**, **Hansel C.** Toward a neurocentric view of learning. *Neuron* 95: 19–32, 2017. doi:10.1016/j.neuron.2017.05.021.

178. **Lisman J**, **Cooper K**, **Sehgal M**, **Silva AJ.** Memory formation depends on both synapse-specific modifications of synaptic strength and cell-specific increases in excitability. *Nat Neurosci* 21: 309–314, 2018. doi:10.1038/s41593-018-0076-6.

179. **Govindarajan A**, **Israely I**, **Huang SY**, **Tonegawa S.** The dendritic branch is the preferred integrative unit for protein synthesis-dependent LTP. *Neuron* 69: 132–146, 2011. doi:10.1016/j.neuron.2010.12.008.

180. **Magee JC**, **Johnston D.** Characterization of single voltage-gated Na$+$ and Ca^{2+} channels in apical dendrites of rat CA1 pyramidal neurons. *J Physiol* 487: 67–90, 1995. doi:10.1113/jphysiol.1995.sp020862.

181. **Chen X**, **Johnston D.** Properties of single voltage-dependent K$+$ channels in dendrites of CA1 pyramidal neurones of rat hippocampus. *J Physiol* 559: 187–203, 2004. doi:10.1113/jphysiol.2004.068114.

182. **Chen X**, **Johnston D.** Constitutively active G-protein-gated inwardly rectifying K$+$ channels in dendrites of hippocampal CA1 pyramidal neurons. *J Neurosci* 25: 3787–3792, 2005. doi:10.1523/JNEUROSCI.5312-04.2005.

183. **Tzilivaki A**, **Kastellakis G**, **Poirazi P.** Challenging the point neuron dogma: FS basket cells as 2-stage nonlinear integrators. *Nat Commun* 10: 3664, 2019. doi:10.1038/s41467-019-11537-7.

184. **Colbert CM**, **Johnston D.** Axonal action-potential initiation and Na$+$ channel densities in the soma and axon initial segment of subicular pyramidal neurons. *J Neurosci* 16: 6676–6686, 1996. doi:10.1523/JNEUROSCI.16-21-06676.1996.

185. **Spruston N**, **Schiller Y**, **Stuart G**, **Sakmann B.** Activity-dependent action potential invasion and calcium influx into hippocampal CA1 dendrites. *Science* 268: 297–300, 1995. doi:10.1126/science.7716524.